University of Alberta

Simulation of Impact Testing of Implant/Abutment System

by

Simon William Jones

A thesis submitted to the Faculty of Graduate Studies and Research in partial fulfillment of the requirements for the degree of Master of Science.

Department of Mechanical Engineering

Edmonton, Alberta
Fall 2005

0-494-09201-7

Library and Archives Canada

Published Heritage Branch

395 Wellington Street
Ottawa ON K1A 0N4
Canada

Bibliothèque et Archives Canada

Direction du Patrimoine de l'édition

395, rue Wellington
Ottawa ON K1A 0N4
Canada

Your file Votre référence
ISBN:
Our file Notre reference
ISBN:

NOTICE:
The author has granted a non-exclusive license allowing Library and Archives Canada to reproduce, publish, archive, preserve, conserve, communicate to the public by telecommunication or on the Internet, loan, distribute and sell theses worldwide, for commercial or non-commercial purposes, in microform, paper, electronic and/or any other formats.

The author retains copyright ownership and moral rights in this thesis. Neither the thesis nor substantial extracts from it may be printed or otherwise reproduced without the author's permission.

AVIS:
L'auteur a accordé une licence non exclusive permettant à la Bibliothèque et Archives Canada de reproduire, publier, archiver, sauvegarder, conserver, transmettre au public par télécommunication ou par l'Internet, prêter, distribuer et vendre des thèses partout dans le monde, à des fins commerciales ou autres, sur support microforme, papier, électronique et/ou autres formats.

L'auteur conserve la propriété du droit d'auteur et des droits moraux qui protège cette thèse. Ni la thèse ni des extraits substantiels de celle-ci ne doivent être imprimés ou autrement reproduits sans son autorisation.

In compliance with the Canadian Privacy Act some supporting forms may have been removed from this thesis.

While these forms may be included in the document page count, their removal does not represent any loss of content from the thesis.

Conformément à la loi canadienne sur la protection de la vie privée, quelques formulaires secondaires ont été enlevés de cette thèse.

Bien que ces formulaires aient inclus dans la pagination, il n'y aura aucun contenu manquant.

Canada

Dedication

To my family.

Abstract

With the increased use of percutaneous implants for head and neck reconstruction there is an ongoing need for clinically efficient techniques to monitor fixture integrity. Mechanical impact testing is gaining popularity as it does not suffer from the limitations associated with conventional diagnostic techniques. This study documents a Finite Element Analysis which simulates an impact test using contact elements in a transient analysis. The model contains a specified interface between the simulated implant and bone which allows analysis of potential clinical situations including loss of osseointegration, loss of bone margin height and development of a soft connective tissue layer at the bone-implant interface. Three important results were determined:

- Clinical changes in the integrity of the interface should be detectable from the frequency response changes
- The higher frequency visible on the raw accelerometer signal appears to be a second natural frequency of the system
- The second natural frequency shows promise for providing additional information as to the condition of the interface

Acknowledgments

I would first like to sincerely thank a few individuals who have guided me through the mine field of higher education.

Dr. Faulkner — for believing in me when I couldn't do it myself

Dr. Fyfe — for being a friend as well as a mentor

Dr. Raboud — for every challenging question that made me a little wiser

I would also like to thank the people who have joined me during morning rants and afternoon meltdowns.

Jody — for showing me life as a grad student is more about life than grad studies

The Good Vibes Crew (Ryan, Quenton, David, Ryan, Kristin) — for sacrificing their productivity to play frisbee with me (and pool, and cards, and ...)

Table of Contents

1 Introduction **1**
1.1 Introduction and Literature Review 1
1.2 Thesis Outline 7

2 Derivation of the Salient FEA Model Parameters **9**
2.1 Percutaneous Bone Anchored Implants 9
2.2 Validation of the *In Vitro* Model 11

3 Construction and Validation of the Finite Element Model **17**
3.1 Finite Element Analysis Basics 17
3.2 Approximate Analysis of Periotest® Accelerometer Signal . . . 19
3.3 Analytical Verification of Finite Element Model 21
3.3.1 Modal Analysis Verification 23
3.3.2 Transient Analysis Verification 24
3.4 *In Vitro* Simulation 27
3.4.1 Simulating the *In Vitro* Model using Modal Analysis . 28
3.4.2 Simulating the *In Vitro* Model using Transient Analysis 32
3.4.2.1 Higher Frequency Investigation 35
3.4.2.2 Sensitivity of Transient Analysis to Defining Variables 38
3.4.3 Choosing the "Better" Model 41
3.5 The Use of Contact Elements in the Transient Analysis 42
3.5.1 Contact Status and Pinball Radius 42
3.5.2 Importance of Time Step Intervals 43
3.5.3 Importance of Element Size 44
3.5.4 Contact Algorithms 44

4 FEA Simulation Results **48**
4.1 Simulating the Changes in the Interface Layer 49
4.1.1 Results of Changes in the Interface Layer 49

5 Conclusions **58**

References **60**

A FEA Example **66**

B Modal Participation Factors from a Continuous System Approximation **68**
B.1 Governing Equation 68
B.2 Constructing the Stiffness Matrix 69
B.3 Constructing the Mass Matrix 71
B.4 Matrix Partitioning for Coordinate Reduction 71
B.5 Comparison to Continuous Cantilever 72
B.6 Determining Modal Participation Factors 74

C Subspace Modal Solver **77**
C.1 Gram-Schmidt Orthogonalization 79

D Transient Solver **81**

E Analytical Second Natural Frequency **84**
E.1 Boundary Conditions 85
E.2 Solve for (βL) 86

F ANSYS and MATLAB Code **89**
F.1 MATLAB Code for Analytical Analysis of Modal Participation Factors 89
F.2 ANSYS Code for 3-D Modal Verification Model 93
F.3 ANSYS Code for 3-D Transient Verification Model 95
F.4 ANSYS Code for Modal Analysis Model - Top Strike 97
F.5 ANSYS Code for Osseointegration Loss - Dental 102

List of Tables

2.1 Model Properties and Dimensions 15
2.2 Frequency Response Comparison for *In Vivo* and *In Vitro* . . 15
2.3 Frequency Response at Five Striking Heights for *In Vitro* Model 16

3.1 Natural Frequency Comparison of Continuous and Finite Systems 19
3.2 Modal Participation Factors for First Three Natural Frequencies 21
3.3 Theoretical First and Second Natural Frequencies of Verification Model 22
3.4 Modal Analysis Verification Comparison - Frequency 24
3.5 Modal Analysis Verification Comparison - Mode Shape 25
3.6 Transient Analysis Verification Comparison 26
3.7 Transient Analysis Verification Comparison - Mode Shape . . 27
3.8 First and Second Natural Frequency Comparison for Cantilevered Aluminium Post 38

4.1 Model Properties for Extraoral Prostheses (BAHA) 50

B.1 (βL) Comparisons of Continuous and Finite Systems 72
B.2 Modal Participation Factors for First Three Natural Frequencies 76

List of Figures

1.1 Typical Implant/Abutment System [1] 2
1.2 Periotest® Schematic 4
1.3 Typical Accelerometer Signal 5
1.4 Schematic of Resulting Motion of Implant and Rod During A Normal Strike 5

2.1 Components of a Typical Implant System 10
2.2 Schematic of Implant System Including Important Terms . . . 11
2.3 Output from an Impact Test *In Vivo* 12
2.4 Schematic of Simplified *In Vitro* Model 13
2.5 Testing Apparatus for *In Vitro* Model 14
2.6 Output from an Impact Test *In Vitro* 14

3.1 Model Approximating Elastically Supported Beam with Point Mass 20
3.2 First Three Expected Mode Shapes 20
3.3 Finite Element Representation of Beam Used for Verification . 22
3.4 First and Second Theoretical Mode Shapes of Verification Model 23
3.5 Modal Verification Model 24
3.6 First Mode Shape of FEA Verification Model 25
3.7 Second Mode Shape of FEA Verification Model 25
3.8 Diagram Depicting the Location of Dense Elements Simulating a Point Mass 29
3.9 Modal Analysis Model With No Interface Layer 29
3.10 Comparison of Modal Analysis with No Interface Layer to *In Vitro* Model (First Mode) 30
3.11 Comparison of Modal Analysis with Interface Layer to *In Vitro* Model 31
3.12 Mode Shapes for Modal Analysis (1-10) 33

3.13 Transient Analysis Model 34
3.14 Comparison of Transient Analysis to *In Vitro* Model 36
3.15 Comparison of Higher Frequency from Transient Analysis to *In Vitro* Model 36
3.16 Typical Transient Analysis Signal 37
3.17 Sensitivity Results for Altering Interface Young's Modulus . . 39
3.18 Sensitivity Results for Altering Interface Thickness 39
3.19 Sensitivity Results for Altering Aluminium Post Density . . . 40
3.20 Sensitivity Results for Altering Aluminium Post Young's Modulus 40
3.21 Sensitivity Results for Altering Mass of Impact Rod 41
3.22 Surface to Surface Contact Depiction 43
3.23 Cantilever Beam Meshed with Two Elements 45

4.1 Schematic of Simplified BAHA Model 50
4.2 First Natural Frequency Comparison for Simulated Loss of Osseointegration and Loss of Bone Margin Height (Oral Implants) 52
4.3 Second Natural Frequency Comparison for Simulated Loss of Osseointegration and Loss of Bone Margin Height (Oral Implants) 52
4.4 First Natural Frequency Comparison for Simulated Loss of Osseointegration and Loss of Bone Margin Height (BAHA Implants) 53
4.5 Second Natural Frequency Comparison for Simulated Loss of Osseointegration and Loss of Bone Margin Height (BAHA Implants) 53
4.6 First Mode Response to Changing Interface Stiffness - Oral Implant 54
4.7 Second Mode Response to Changing Interface Stiffness - Oral Implant 54
4.8 First Mode Response to Changing Interface Stiffness - BAHA Implant 55
4.9 Second Mode Response to Changing Interface Stiffness - BAHA Implant 55
4.10 Filtered FFT Output for A Simulated Impact Test on BAHA Model with 1mm of Osseointegration Loss 57
4.11 Filtered FFT Output for A Simulated Impact Test on BAHA Model with 1.5mm of Osseointegration Loss 57

A.1 FEA Example Rod 66
A.2 Finite Element Representation of Rod 67

B.1 Cantilever with Spring Attached to Ground 70
B.2 Model Approximating Elastically Supported Beam with Point Mass 73
B.3 First Three Expected Mode Shapes 74
B.4 Momentum Diagram 75

E.1 Analytical Model to Verify Second Mode of Vibration 84
E.2 FBD/MAD of Point Mass 85
E.3 Plot of Residuals from E.12 Used to find βL Values 88

Chapter 1

Introduction

1.1 Introduction and Literature Review

Bone anchored implants are increasingly being utilized in a broad range of oral and extraoral reconstructions as foundations for dental arches, portions of the head (ears, eyes, noses) and as part of a Bone Anchored Hearing Aid (BAHA) system. A typical implant and abutment system used for percutaneous reconstructions is shown in Figure 1.1. These implants are typically 3-6 mm in diameter and range in length from 3-4 mm (BAHA and facial applications) to 7 - 20 mm (dental reconstructions). The quality of the supporting bone can be assessed qualitatively or through bone density studies from radiographs. The condition of the bone-implant interface, however, including the implant threads and the adjacent tissue undergoing remodelling, can have a dramatic effect on the success or failure of the system and is much more difficult to evaluate. The direct structural and functional connection between ordered, living bone and the surface of a load-carrying implant is defined as osseointegration [1]. This process begins immediately after the implant has been installed. If this does not occur, the development of connective soft tissue in the bone-implant interface may begin and can lead to failure of the implant. The status of the implant-bone interface during this crucial time is extremely important in evaluating when the implant can be put into service (loaded) or whether further healing is necessary. In addition, over time osseointegration can deteriorate and/or the degree of bone in contact with the implant surface can reduce. As a result of these potential clinical conditions, there is an ongoing need to monitor the "health" or

integrity of the bone-implant interface from initial installation throughout the life of the implant. Although implant survival rates are high in many applications, it is vital to be able to determine if any change in the health of this interface occurs [2, 3].

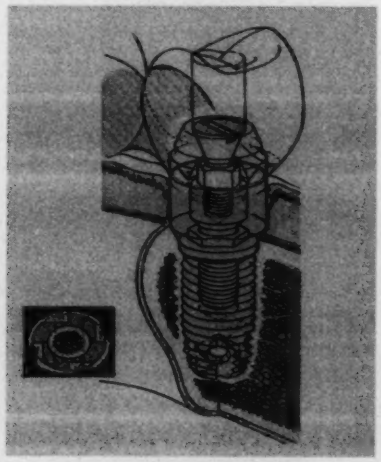

Figure 1.1: Typical Implant/Abutment System [1]

Conventional diagnostic techniques, including radiography and magnetic resonance imaging are limited as a means of determining the status of osseointegration. While they are able to evaluate bone quality, implant shielding causes poor resolution at the implant-tissue interface limiting the ability to monitor this vital area [4, 5]. Additionally, using radiography, the changes in bone are often well advanced before becoming evident on radiographic images. Other techniques such as measuring removal torque are too invasive to be used in either the operating room or for clinical visits [6]. As a result, dynamic mechanical testing methods have been proposed and are presently in use. These mechanical techniques are all, in one form or another, based on determining the resonant frequency of the implant-tissue system. As the resonant frequency is dependent on the manner in which the implant is supported by the surrounding biological tissue, changes in this resonant frequency (perhaps coupled with changes in the internal damping) should be linked to changes in the status of this interface [7]. For instance, if the

bone stiffness increases, the implant will be held more securely therefore the frequency should go up. If there is a loss in bone margin height the implant will be less secure therefore the frequency should go down. This, of course, assumes that there are no other changes in the implant system that may overshadow those in the interface.

The only commercially available system developed specifically for osseointegrated implant assessments is the Osstell®. This system employs a transducer mounted on the implant or the abutment. The transducer excites the system over a range of frequencies and simultaneously monitors the resulting response to determine the resonant frequency of the implant-tissue-transducer system. The results of several investigations using this resonance frequency analysis (RFA) system have reported varying success in identifying changes in the implant status [8–12]. One of the major drawbacks to the Osstell® system is that a large majority of the oral based implant restorations use non-recoverable, cemented, fixed prostheses and the status of the implant cannot be monitored once the prosthesis is in place.

Alternative techniques to the Osstell® system are based on an impact technique. Early attempts using a transient approach are outlined in the thesis by Meredith [13]. More recently, Elias, Brunski and Scarton proposed the use of an instrumented impact hammer to evaluate the mechanical impedance variations caused by interface changes [5]. Huang and co-workers also used an impact hammer to excite the implant-abutment unit [14]. The resonant frequency of the freely vibrating system was determined from the acoustic signal obtained from a microphone mounted in close proximity to the abutment.

An alternate system, the Periotest®, utilizes a handpiece containing an accelerometer and a signal processing unit to monitor and interpret implant motion [15, 16]. The Periotest® hand piece contains a metal rod, of approximately 9 grams, that is accelerated towards the implant-abutment via an electromagnet, as depicted in Figure 1.2 [17]. The acceleration response of the rod, while in contact with the implant-abutment, is measured using the accelerometer attached to the rear of this rod. The Periotest® was originally developed to measure the mobility of natural dentition but numerous investigators have considered its application for implants with varying degrees of success [18–20]. It appears some of the inconsistencies are due to variations in the protocol for using the system and some from the imprecision in the processing of the accelerometer signal [21]. However there are benefits to this system. The Periotest® hand piece provides a convenient means to dynami-

cally excite the implant-abutment system in areas that may be too cramped to utilize RFA or impact hammer devices. Also, the Periotest® handpiece can be used on implant-abutment systems with non-recoverable, cemented restorations. As well, the output signal from the accelerometer may contain information unavailable to the RFA systems which can be more completely utilized to determine the status of the interface layer. For example, the hand piece has recently been adapted for use in a system designed to measure the damping capacity of materials [22].

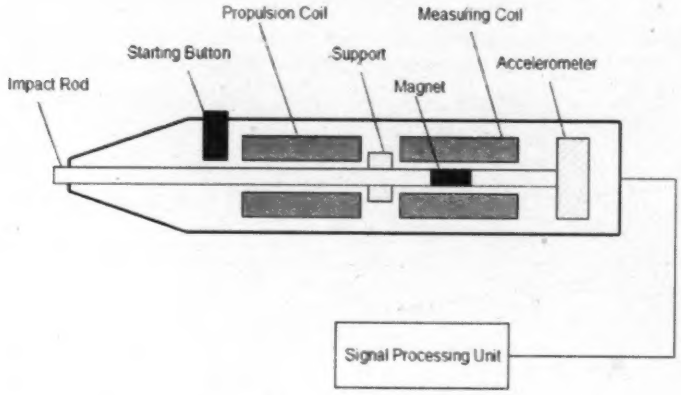

Figure 1.2: Periotest® Schematic

In the Periotest® system, the raw accelerometer signal is filtered and processed to yield a quantitative measure of mobility related to the Miller Mobility Index for natural dentition [15]. An example of the signal before and after conditioning is shown in Figure 1.3 with a schematic diagram of the corresponding motion of the implant and rod shown in Figure 1.4. The time required for the filtered accelerometer signal to return to its zero value has been termed the contact time, CT, depicted in stages 1 through 3 in Figure 1.4. In the processing unit of the Periotest® this contact time is used to calculate the so-called Periotest® Value (PTV).

If the system is modelled as a single degree of freedom vibration system, the contact time can be thought of as a half period and the natural frequency

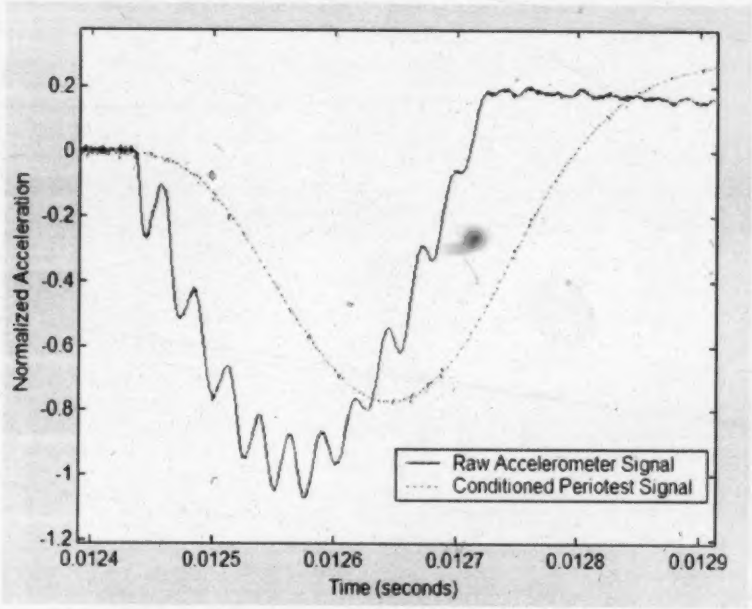

Figure 1.3: Typical Accelerometer Signal

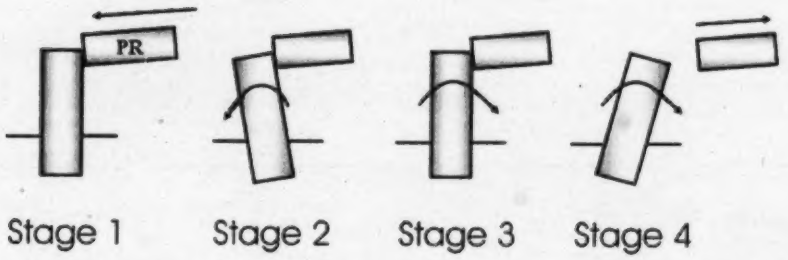

Figure 1.4: Schematic of Resulting Motion of Implant and Rod During A Normal Strike

of the implant-tissue-Periotest® rod combination is simply

$$p = \frac{1}{2 \cdot CT} \tag{1.1}$$

In terms of the natural frequency, the PTV can be expressed as

$$PTV = 50000\left(\frac{1}{2p}\right) - 21.3 \tag{1.2}$$

Figure 1.3 shows that there can be considerable differences between the raw accelerometer signal and the conditioned signal from the Periotest®. While these differences may not be important for natural dentition as the range of PTV values is relatively large (-6 to 50), they have more significance for implant-abutment systems where the majority of results have PTV's over a much more limited range (-8 to 2).

The purpose of the present work is to further investigate the possibility of using this impact technique to more precisely monitor the status of the bone - implant interface. To accomplish this, a more detailed understanding of how the geometric and clinical variables affect the response is necessary. For instance, do variables such as osseointegration levels and loss of bone margin height have an appreciable effect on the overall response? To investigate these issues, the raw accelerometer signal (see Figure 1.3) will be more fully investigated as it appears to have higher frequency components that could be potentially used to glean more information about the "health" or integrity of the implant interface. There has been some debate as to what this apparent higher frequency represents. Elias [5] stated it was due to partial separation between the impact tool and the implant, resulting in a "bouncing" effect. It has also been hypothesized this frequency is merely electrical noise on the accelerometer signal or the second mode of vibration of the implant-tissue system. This will be investigated in the following chapters to understand the source of this component of the signal and if it can be used to better understand the status of the interface.

In order to interpret the signal from the accelerometer and relate it to the condition of the interface, it is necessary to understand the role of each of the components of this dynamic system and its effect on the output signal. To this end, Finite Element Analysis (FEA) is used as it allows a means to dynamically model the implant-abutment with considerable detail. This includes modelling the supporting structure including the introduction of a specific interface layer that can have different properties.

FEA has been used by numerous researchers to investigate the implant-tissue connection. Many studies are concerned with stress and strain in the interface layer. The goal can be to determine the maximum strain due to occlusal loading [23–30] or to optimize implant design in order to minimize stress [31–36]. The other vein of research focuses on dynamic modelling which attempts to find relationships between natural frequencies and the surrounding conditions of the implant. For example, Huang et al. [37] utilized modal analysis of the implant-tissue system to investigate how bone type and bone density affects resonant frequency. Williams et al. [38] utilized force harmonic response and localized impulse excitation to improve a model investigating the effect of bone type on natural frequency. In the current work, FEA is used to produce a more thorough dynamic model of the implant-abutment by including the impact of the Periotest® rod with the implant.

1.2 Thesis Outline

Chapter 2 details how the salient features of the FEA model were derived from the *in vivo* and *in vitro* situations, beginning with a brief overview of the components and placement of percutaneous implants. This leads to a discussion on the characteristics of the implants and abutments that are being investigated *in vivo* and the typical signals acquired during patient testing. A comparison between the filtered Periotest® signal and the raw accelerometer signal is also included. A description of the *in vitro* model and testing apparatus is described and compared to the *in vivo* situation.

Chapter 3 focuses on the finite element simulation of the *in vitro* model. An overview of FEA basics is followed by a simplified numerical model used to evaluate the plausibility of two natural frequencies being visible on the accelerometer signal. This leads to a review of the process used to verify the software produces accurate results in both two and three-dimensions, including comparisons to analytical and experimental results. The validity and usefulness of two FEA models (a model using modal analysis and a model using impact analysis) is debated and the superior model is chosen. This requires an overview of certain techniques utilized by the FEA software including modal analysis solvers, transient analysis solvers and contact element theory. The most appropriate model is verified using extensive comparisons to analytical and *in vitro* results.

Chapter 4 simulates three, more complex cases which would be difficult

to simulate *in vitro*. These include determining the response to a loss of osseointegration, a decrease in bone margin height and a general change in implant interface stiffness simulating the development of connective soft tissue. The results of these three cases are then discussed with a view to better understand the *in vivo* situation.

Chapter 2

Derivation of the Salient FEA Model Parameters

In order to finally develop a numerical model which simulates the *in vivo* situation, an *in vitro* experimental model was developed. This was done to identify the salient features to be included in the finite element model.

2.1 Percutaneous Bone Anchored Implants

The percutaneous implant system is made up of three major components: the fixture, the abutment and the connection screw (Figure 2.1). For clarity, the term "fixture" and "implant" will be used interchangeably in this thesis. These components are generally made from titanium, with the fixture having a defined finish and geometry thought to create a firm, intimate and lasting connection with the host bone [2]. The general procedure for installation begins with placement of the fixture. The fixture is installed by drilling a hole into the host bone, sized according to the manufacturer's specifications, into which the fixture is inserted to the required depth. Depending on the application, the fixture can be covered with skin or a healing abutment can be attached and the system left to heal for a period of weeks or months, depending on the clinical practice. Once the fixture is deemed ready, the working abutment and prosthesis are attached and loading begins.

During this healing period, it is generally believed that a process of osseointegration takes place. Osseointegration has been defined as a process of bone ingrowth at the implant surface to create a secure bond with the

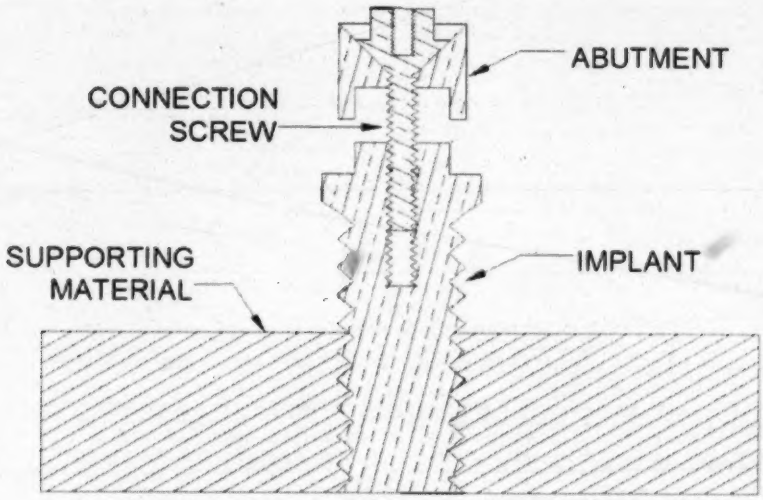

Figure 2.1: Components of a Typical Implant System

bone [39]. This processes creates a bond which allows tensile forces to be sustained between the fixture and the surrounding tissue. This greatly increases the effective stiffness of the implant-tissue system allowing the implant to withstand greater loads without threatening the integrity of the fixture.

Figure 2.2 has been included in order to clarify various descriptive terms used herein. The abutment height is the vertical length of the abutment extending past the top of the implant. Engagement length is the vertical length of the implant that is surrounded by bone. The interface layer is a thin layer which simulates the implant threads and the adjacent tissue undergoing remodelling. Striking height is the vertical distance between the surface of the bone and the point of contact between the impact rod and the abutment.

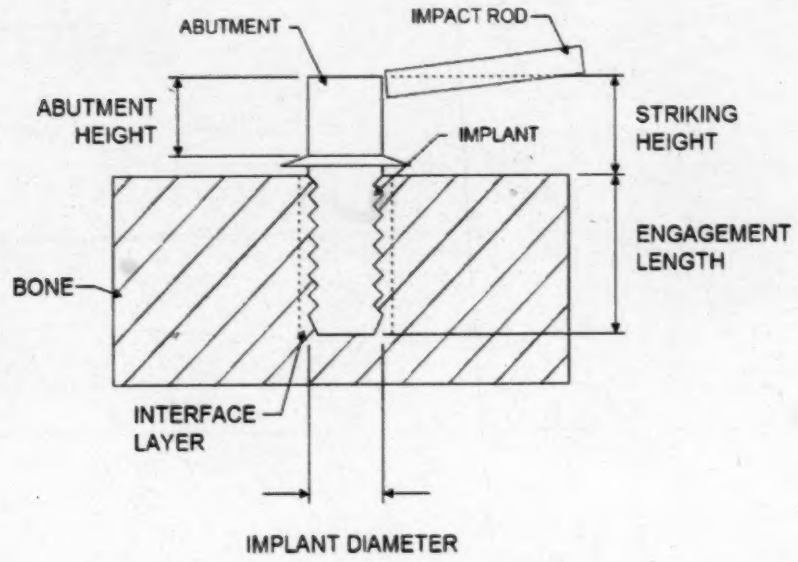

Figure 2.2: Schematic of Implant System Including Important Terms

2.2 Validation of the *In Vitro* Model

While there are a plethora of implant systems, simulations were focused on the Brånemark implant systems, widely used in typical oral restorations and BAHA placements, to gain an appreciation of the range of variations expected in clinical situations. For the oral case a 9 mm long, 4 mm in diameter implant was chosen along with a 10 mm abutment, since a prosthetic tooth is typically about 1 *cm* high. The extra-oral case used a 4 mm long, 3.75 mm in diameter implant with 5 mm abutment, typical for the BAHA system.

Figure 2.3 depicts the typical response of an oral implant-abutment system to a Periotest® strike at the top of the abutment. The two curves represent the raw accelerometer signal and the conditioned Periotest® signal. The important differences include the filtering and subsequent elongation of the contact time of the processed signal.

The conditioned signal has been filtered to remove the higher frequency

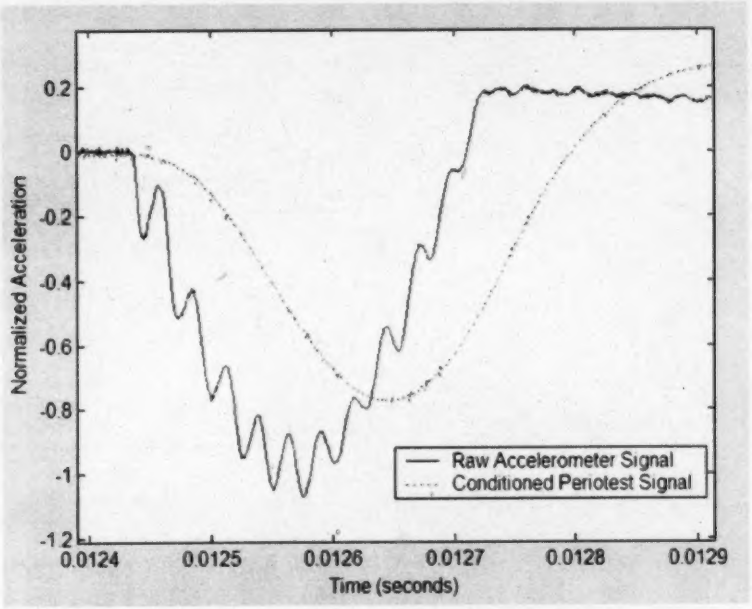

Figure 2.3: Output from an Impact Test *In Vivo*

seen in the raw signal. This allows the Periotest® processing unit to calculate the Periotest® Value (PTV), which is a measure of the contact time as outlined in the introduction. This filtering, however, elongates the contact time, artificially reducing the stiffness of the supporting tissue. Also, this elongation is not constant and appears to be most prevalent at low PTV (high stiffness) which is the case for implants. Since the conditioned signal is both altering the contact time and eliminating potentially useful information, the unadulterated signal was saved during all *in vivo* tests using a multi-channel A/D data acquisition system (InstruNet Model 100 A/D 8 Bit I/O, GW Instruments Inc, Somerville, MA, USA) sampling at 167 kHz. The signals were later processed in MATLAB® (The MathWorks Inc, Natick, MA, USA) using custom FFT software to determine the frequencies present.

Since the host bone has constantly changing material properties due to ongoing remodelling, it would be difficult to verify a numerical simulation

using the *in vivo* situation. However, a material named FRB-10 has a modulus (8.4 GPa) in the reported range of cortical bone (5 - 20 GPa) [39]. Thus, to assist in the development of a measurement protocol and the validation of analytical and numerical models, the *in vitro* experimental model shown schematically in Figure 2.4 was developed using this material. This model allowed the majority of the variables affecting the response of the implant-abutment to a impact test to be varied to determine how specific variables affect the response of the system.

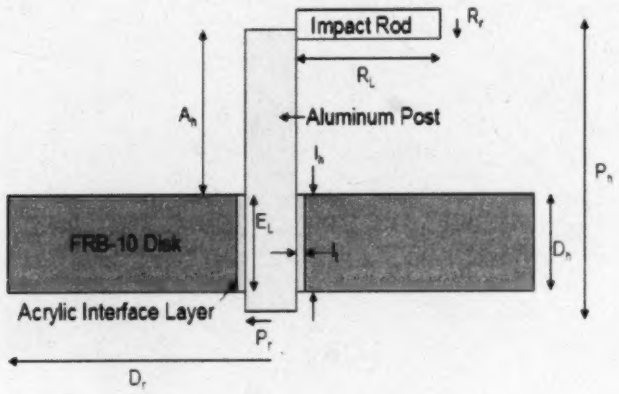

Figure 2.4: Schematic of Simplified *In Vitro* Model

The *in vitro* model is approximately the size of an oral implant-abutment system. It consists of an aluminum post fixed with acrylic into the center of a disk of FRB-10(Measurements Group Inc, Raleigh, NC, USA). The mechanical properties and sizes of these components are given in Table 2.1. The thickness of the interface (0.38 mm) is relatively large in order to account for the root diameter of the implants threads as well as the tissue in close proximity to the implant.

The disk was clamped in a circular trough which was in turn mounted in a clamping device that also supported the clamped Periotest® handpiece (Figure 2.5). The clamped handpiece was mounted on a microscope stage to allow adjustment of the position of the rod relative to the abutment.

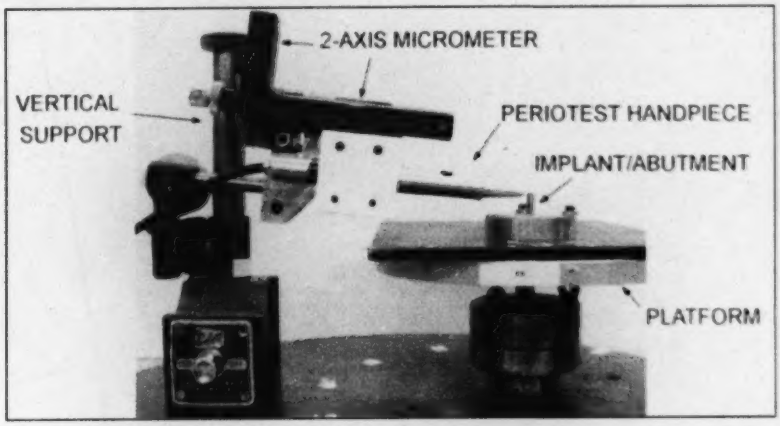

Figure 2.5: Testing Apparatus for *In Vitro* Model

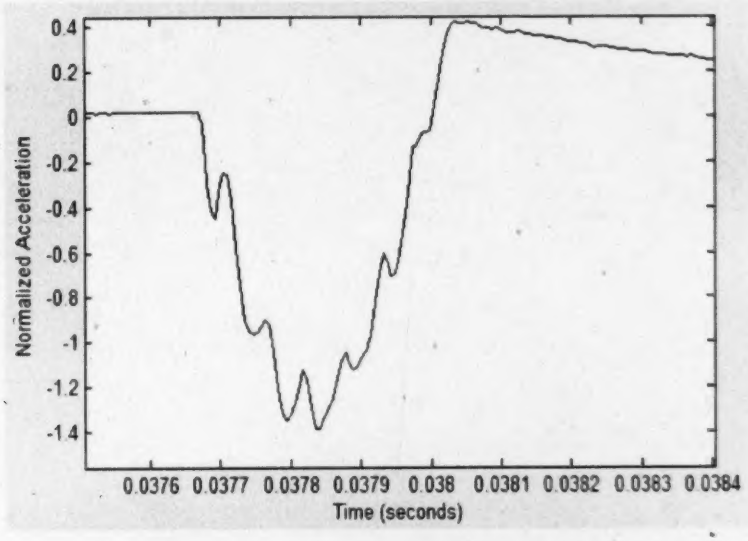

Figure 2.6: Output from an Impact Test *In Vitro*

Table 2.1: Model Properties and Dimensions

Post Radius (P_r)	2 mm	Post Height (P_h)	20 mm
Abutment Height (A_h)	10 mm	Engagement Length (E_L)	9 mm
Interface Thickness (I_t)	0.38 mm	Interface Height (I_h)	9 mm
Disk Radius (D_r)	20 mm	Disk Height (D_h)	9 mm
Periotest® Rod Radius (R_r)	1 mm	Periotest® Rod Length (R_L)	20 mm
Component	Young's Modulus (GPa)	Poisson's Ratio	Density (kg/m^3)
FRB Disk	8.4	0.31	1800
Aluminium Post	73	0.32	2800
Acrylic Interface Layer	0.5	0.30	1800
Periotest® Rod	200	0.30	9.4 grams

A typical response of the *in vitro* model to an impact at the top of the post is shown in Figure 2.6. Comparison of this response to that of the *in vivo* response shown in Figure 2.3 suggests that the signals are similar as both appear to be made up of a half period of a low frequency with a higher frequency superimposed. Signals were analyzed using the custom FFT software and produced the results shown in Table 2.2.

Table 2.2: Frequency Response Comparison for *In Vivo* and *In Vitro*

Experiment	Low Frequency (Hz)	High Frequency (kHz)
In Vivo - 10mm abutment 9mm implant, 4mm diameter	1900	27.0
In Vitro - 19 mm post 9mm engagement, 4mm diameter	2100	30.0

As the comparisons were both qualitatively and quantitatively similar, the *in vitro* model appears to capture the essence of the *in vivo* response. However, the *in vitro* model is limited in its ability to simulate more complex

cases of failure found *in vivo*. Thus a finite element model was created which could be verified using the *in vitro* model and then expanded to simulate these *in vivo* failure situations. The response of the *in vitro* model to impact tests at five striking heights, starting at the top and decreasing in 1 mm intervals, were recorded in Table 2.3 for use in the verification process described in Chapter 3.

Table 2.3: Frequency Response at Five Striking Heights for *In Vitro* Model

Striking Height (mm)	Low Frequency (Hz)	High Frequency (kHz)
10 (Top)	1790	39.8
9	1910	42.7
8	2077	42.3
7	2307	40.5
6	2492	38.9

Chapter 3

Construction and Validation of the Finite Element Model

As described above, the use of impact testing for implants is effective for determining changes in the supporting structure by measuring changes in the natural frequency. While essentially all the previous studies assume the response of the implant - abutment is equivalent to that of a one degree of freedom vibrating system, the actual response indicates what appears to be a second frequency. In order to determine if this second frequency may be due to excitation of a higher mode of vibration which may be useful in evaluating the health of the implant, finite element analysis was utilized.

After a brief overview of the finite element method, a simplified finite element model of the system is developed and verified against an analytical solution to evaluate whether or not higher modes could be excited and would be distinguishable in the impact test. As it appears this is the case, a more extensive finite element model was developed to explore the utility of the higher mode. Two techniques, a modal and a transient analysis, are compared to evaluate which method yields the better results when compared with the *in vitro* and *in vivo* situations.

3.1 Finite Element Analysis Basics

FEA is a process where the original continuous structure is divided into many smaller, finite elements. Each of these h-elements is a linear or quadratic system described by the element's governing equations. The elements are

defined by nodes, generally found on the ends or corners of the elements. Consecutive elements share nodes along common boundaries creating continuity across the entire body. A change in one element therefore affects the initial or boundary conditions of the surrounding elements. By minimizing the internal energy of the system it is possible to determine the final configuration of the elements given the initial and boundary conditions of the original body. Appendix A contains a simple example to illustrate the FEA method.

Although FEA has some distinct advantages over analytical techniques, one must be aware of its limitations. For example, it is advantageous that material properties, such as Young's modulus, density and Poisson's ratio, are "built into" the elements. Analytical methods, in the case of vibrations for instance, may require approximations for spring stiffness or inertial properties. Using FEA these properties are calculated during the solution phase so they are accurate for the input geometry and material properties of the elements. However, there is the matter of the number of elements used to discretize the geometry. Consider a rigidly fixed, three-dimensional cantilever beam with a square cross section that is loaded vertically at the free end. Although a single 3-D brick element can accurately capture the geometry of the model, it will not produce the analytically expected deflections. It requires a fine discretization to capture the changing slope of the beam. However, the more elements, the larger the global stiffness matrix, which has a direct correlation to processing time. This is analogous to a Fourier Series approximation. The more higher order terms that are included, the more accurate the solution but with increased calculation difficulties. Therefore, one looks to find the optimum balance between accuracy of solution with processing time. This process is generally termed "testing for convergence". By increasing the number of elements and comparing to the previous solution, one can determine the minimum required number of elements to come within a prescribed criterion of the converged solution. Fewer elements will result in high amounts of solution error while more elements will result in additional processing time. Testing for convergence is a necessary step in any finite element analysis if the results are to be trusted. These concepts are used in the following section while investigating the higher frequency present in the Periotest® accelerometer signal.

3.2 Approximate Analysis of Periotest® Accelerometer Signal

To evaluate whether or not the higher frequency evident in the raw accelerometer signal could be due to excitation of an additional natural frequency, an approximation of the system was used to estimate the modal participation factors of the first three modes. As the completely analytical analysis of the transient loading of a cantilever with a point mass is quite complicated, the system was instead broken into a number of beam segments forming the approximate lumped mass model illustrated in Figure 3.1. The details of this method are given in Appendix B. Table 3.1 compares the first three natural frequencies of a rigidly fixed cantilever ($M = 0$ and $k_s \rightarrow \infty$) solved both analytically and using finite element method, showing that the finite element system converged to the solution of the continuous system:

$$p_n = \frac{(\beta L)_n^2}{2\pi}\sqrt{\frac{EI}{\rho A L^4}} \quad Hz \tag{3.1}$$

where p_n is natural frequency of the n^{th} node, βL is a constant dependent on the desired mode [40], E is Young's modulus of the cantilever, I is the second moment of area about the neutral axis, L is the length of the cantilever, A is the cross sectional area and ρ is the density of the material.

Table 3.1: Natural Frequency Comparison of Continuous and Finite Systems

System	First Natural Frequency (Hz)	Second Natural Frequency (Hz)	Third Natural Frequency (Hz)
Continuous	286	1791	5014
Finite	284	1780	4985

The results show the first three modes of a 200 degree of freedom (DOF) model converged to be within 0.6% relative error for the case with the support being rigid and the free end having no mass.

Having shown the finite DOF solution converges to the analytical solution for a simple cantilever, this method was expanded to the case of an elastically supported beam with a point mass, with the assumption that the solution

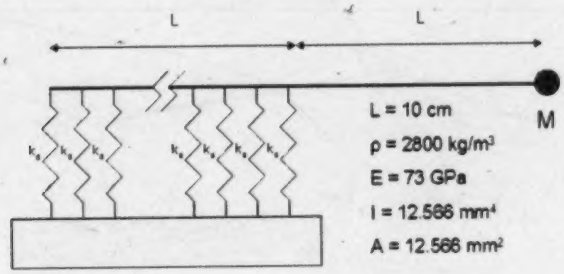

Figure 3.1: Model Approximating Elastically Supported Beam with Point Mass

would again converge to the continuous system solution. In this case M was increased to 13 times the mass of the beam to simulate the mass of the impact rod and k_s was decreased until the first two mode shapes were rigid body modes, as predicted by Hurst [41]. The first three resultant mode shapes are depicted in Figure 3.2. Again the solution converged below 1% with 200 DOF. Using modal superposition for the transient impact, the modal participation factors (MPF) for the first three modes, shown in Table 3.2, indicate that the first mode had an MPF 24 times that of the second and 1400 times that of the third.

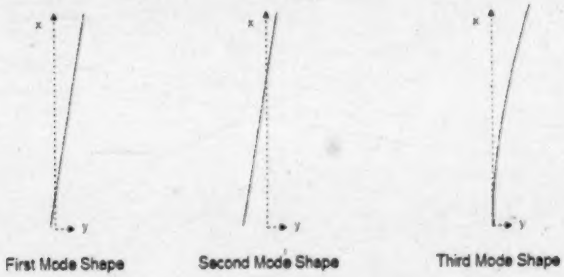

Figure 3.2: First Three Expected Mode Shapes

As a result, it is expected that the second mode of vibration would have

Table 3.2: Modal Participation Factors for First Three Natural Frequencies

Natural Frequency	MPF
$1st$	$3.02\text{x}10^{-2}$
$2nd$	$-1.26\text{x}10^{-3}$
$3rd$	$2.21\text{x}10^{-5}$

a smaller amplitude on an accelerometer signal than would the first. As well, the participation of the third (and subsequent) natural frequencies would be so minor, relative to first mode, that they could be reasonably neglected. The results from this approximation suggest that the higher frequency could plausibly be the second natural frequency and explains why other modes are not observed. The development of a realistic finite element model should then allow a more thorough examination of these modes and how they are affected by changes in the supporting structure.

3.3 Analytical Verification of Finite Element Model

As the first and possibly second natural frequencies of the implant structure during an impact test are under investigation, a verification process was undertaken to ensure the finite element package (ANSYS 7.1, ANSYS Inc, Canonsburg, PA, USA) produced realistic first and second natural frequency results for a simple case that could be solved analytically before constructing more realistic models. It was decided of the four solvers applicable to vibrational analysis (modal, harmonic, spectrum and transient analysis) only the modal and transient analyses would be compared to the analytical solution. Harmonic analysis was not considered since it would utilize the same model as modal analysis but does not conveniently produce mode shapes. Spectrum analysis was not considered since the resultant stress field was not of interest to this research.

The cantilever seen in Figure 3.3 was used to verify the FEA package. The geometry and material properties were selected to yield an analytical solution with a first natural frequency in the same order of magnitude as the *in vivo* and *in vitro* results shown in Table 2.2 yet meeting the "long and

slender" assumption used for the analytical solution (Thomson [42]).

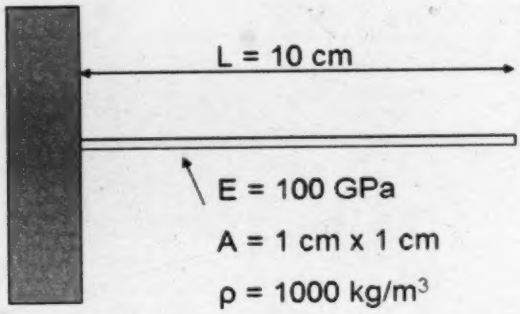

Figure 3.3: Finite Element Representation of Beam Used for Verification

Table 3.3: Theoretical First and Second Natural Frequencies of Verification Model

	βL	Frequency (Hz)
First	1.875	1615
Second	4.694	10123

Table 3.3 contains the first two natural frequencies predicted by Equation (3.1) with the mode shapes seen in Figure 3.4 and described by:

$$\tilde{y}\left(\frac{x}{L}\right) = \cosh\left(\frac{(\beta L)x}{L}\right) - \cos\left(\frac{(\beta L)x}{L}\right) - \sigma\left(\sinh\left(\frac{(\beta L)x}{L}\right) + \sin\left(\frac{(\beta L)x}{L}\right)\right) \tag{3.2}$$

where $\sigma = 0.7341$ for first mode and 1.0185 for second mode [40]. These frequencies and mode shapes will be compared to the results from the modal and transient finite element models detailed below.

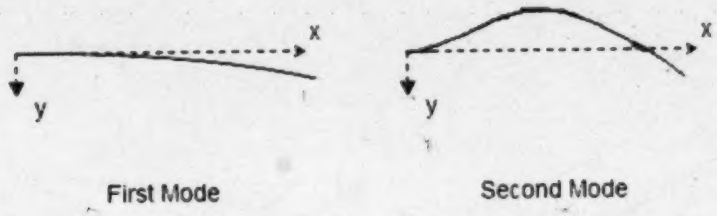

Figure 3.4: First and Second Theoretical Mode Shapes of Verification Model

3.3.1 Modal Analysis Verification

Modal analysis is a method of determining the natural frequencies and mode shapes of a given structure. The finite element method is similar to the analytical method of modal analysis with some slight changes to decrease processing time.

While ANSYS has a number of solver types that can be chosen from for modal analysis, the subspace method was used for this research. The subspace method is the most robust of the solution options since it does not use master nodes to speed up the solution process, thus it reliably converges to a solution. The basic subspace algorithm is outlined in Appendix C, with further details in Bathe [43] and Wilson [44]. In this method, an eigenvalue problem consisting of the mass and stiffness matrices is solved to produce the natural frequencies (eigenvalues) and mode shapes (eigenvectors) of the structure. The difference from the analytical method is that the entire eigenvalue problem does not have to be solved. It is possible to solely extract the first few frequencies, saving huge amounts of processing that would be required to solve the full problem.

The model shown in Figure 3.5 was created for the modal analysis verification using the dimensions in Figure 3.3 with the left face of the beam fully constrained. Sample code can be found in Appendix F, Sections F.2.

The mesh size was reduced until the first natural frequency of the three-dimensional system converged within 1%. The final model consisted of 10000 SOLID45 elements (quadratic elements comprised of 8 nodes having three degrees of freedom at each node: translation in the nodal x, y and z directions [45]). The resulting natural frequencies are compared to the analytical

Figure 3.5: Modal Verification Model

solution in Table 3.4 with the mode shapes compared in Table 3.5 and shown in Figures 3.6 and 3.7.

Table 3.4: Modal Analysis Verification Comparison - Frequency

	First Natural Frequency (Hz)	Second Natural Frequency (Hz)
Analytical Method	1615	10123
Modal Analysis	1611	9664

The relative errors for the first and second natural frequencies of the modal analysis are 0.2% and 4.5% respectively, and the mode shapes are within 1% and 4% respectively, thus the modal analysis method produces reasonable results for this verification problem.

3.3.2 Transient Analysis Verification

As the name implies, transient analysis determines the transient response of the system based on the boundary and initial conditions. Unlike modal analysis, the transient analysis solution type does not calculate natural frequencies directly. To find the natural frequencies, nodal displacements were plotted versus time and analyzed using the custom MATLAB FFT software. While transient analysis is not as direct when determining natural frequen-

Table 3.5: Modal Analysis Verification Comparison - Mode Shape

	Deflection at $x = \frac{L}{3}$ (Normalized)	Deflection at $x = \frac{2L}{3}$ (Normalized)	Deflection at $x = L$ (Normalized)
Analytical Method (1st Mode)	0.166	0.547	1.00
Modal Analysis (1st Mode)	0.166	0.545	0.995
Analytical Method (2nd Mode)	-0.590	-0.423	1.000
Modal Analysis (2nd Mode)	-0.611	- 0.441	0.995

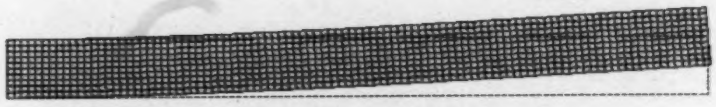

Figure 3.6: First Mode Shape of FEA Verification Model

Figure 3.7: Second Mode Shape of FEA Verification Model

cies, it can be used with non-linear elements, such as contact elements, which the modal analysis method cannot.

Transient analysis solves for the response of the system over some desired time (the response time). As outlined in Appendix D, this response time is broken into discrete intervals, where the system is assumed to be quasi-static. By knowing the initial conditions of displacement, velocity and acceleration at time $t = 0$, it is possible to estimate the displacement, velocity and acceleration at the end of the first time step. The solution to this step is the initial condition vector of the next time step. This process is repeated until the total response time is reached. It is important to test for convergence of the time discretization, reducing the size of the time step until the solution converges below 1%. This is required because the quasi-static assumption would be false if the time step is too large since the acceleration through each time step could not be reasonably assumed linear. ANSYS recommends a time step which is 20 times smaller than the shortest desired period (associated with the highest frequency).

The same model parameters as used previously in the modal analyses were used for the transient analysis with the inclusion of a 100 N load applied vertically at the end of the beam for the first 0.0001 seconds of the total response time (0.001 seconds). An example of the code used to create this model can be found in Appendix F, Section F.3.

Again, the model consisted of 10000 SOLID45 elements and the time step converged within 1% at 5×10^{-6} seconds. The resulting natural frequencies and mode shapes are compared to the analytical solution in Tables 3.6 and 3.7 with the first mode shape again shown in Figure 3.6. It was not possible to determine the second mode shape from the transient analysis since its amplitude was much smaller than the first thus the shape was indistinguishable.

Table 3.6: Transient Analysis Verification Comparison

	First Natural Frequency (Hz)	Second Natural Frequency (Hz)
Analytical Method	1615	10123
3-D Transient Analysis	1611	9677

The relative errors for the first and second natural frequencies of the transient analysis are again 0.2% and 4.5% respectively, and the first mode

Table 3.7: Transient Analysis Verification Comparison - Mode Shape

	Deflection at $x = \frac{L}{3}$ (Normalized)	Deflection at $x = \frac{2L}{3}$ (Normalized)	Deflection at $x = L$ (Normalized)
Analytical Method (1st Mode)	0.166	0.547	1.00
Transient Analysis (1st Mode)	0.165	0.545	0.995

shape is within 1%, with the result that the transient analysis method also produces reasonable results for the three-dimensional verification analysis. As expected, the modal and transient analyses produced equivalent results for given geometry and properties, which added confidence to the finite element method.

3.4 *In Vitro* Simulation

Having shown that ANSYS produces reasonable results for the first and second modes during the verification process, a more realistic model was constructed to simulate the *in vitro* model with confidence that the FEA package could produce comparable results. If this is the case, the FEA model will be expanded to evaluate situations that would be difficult to reproduce *in vitro*.

As both the modal and transient analyses yielded essentially the same results compared to the analytical solution, simulations were done using both techniques to determine which technique is "better" based on:

1) processing time
2) accuracy of solution compared to *in vitro*
3) ease of expanding simulation to model more complex cases

3.4.1 Simulating the *In Vitro* Model using Modal Analysis

The initial modal analysis model was constructed with the dimensions and properties listed in Table 2.1. However, as the acrylic layer is relatively thin, and the stiffness of the FRB disk is relatively low compared to the aluminium post, it was initially hypothesized that the majority of the displacement of the supporting structure would be due to the disk deflecting in the immediate vicinity of the aluminium post. The acrylic layer was thought to have negligible affect on the response of the system and was therefore not included.

In addition, to compare results from the modal analysis to the *in vitro* results, it was necessary to simulate the mass of the Periotest® rod. As the impact rod is assumed to stay in contact with the aluminium post during the strike, the mass of the impact rod was modelled as a point mass. This was accomplished by increasing the density of a small cluster of elements at the striking height, resulting in a total point mass of 9.4 grams. The element cluster is $\frac{1}{8}$ of the semi-annular region 1 mm high between the outer radius of the rod and a radius of 1 mm, as depicted in Figure 3.8. The model shown in Figure 3.9 was the result.

The model was meshed with approximately 14000 tetrahedral elements with mid-sided nodes (SOLID92). These quadratic elements are comprised of 10 nodes having three degrees of freedom at each node: translation in the nodal x, y, and z directions [46]. Convergence testing was performed to ensure the mesh was adequately dense such that solutions did not change more that 1% if the element size was halved. Only one half of the structure was considered due to symmetry as shown. The outer cylindrical surface of the disk was fully constrained to simulate the conditions assumed to be present in the *in vitro* apparatus.

Figure 3.10 is a plot of the results over five striking heights compared to those of the *in vitro* model. It has been reported the Periotest® has 100 Hz resolution, thus error bars representing +/- 50 Hz were included for the *in vitro* data [21]. No error bars were included for the modal analysis data as the frequency was the direct output.

It is apparent that although the results for a strike at the top of the aluminium post are reasonable when compared to the *in vitro* results, the results diverge as the striking height is decreased with a relative error at the lowest strike of 33%. Two possible reasons for these discrepancies were examined.

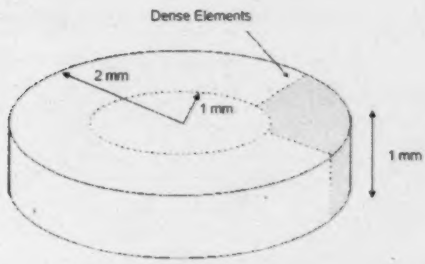

Figure 3.8: Diagram Depicting the Location of Dense Elements Simulating a Point Mass

Figure 3.9: Modal Analysis Model With No Interface Layer

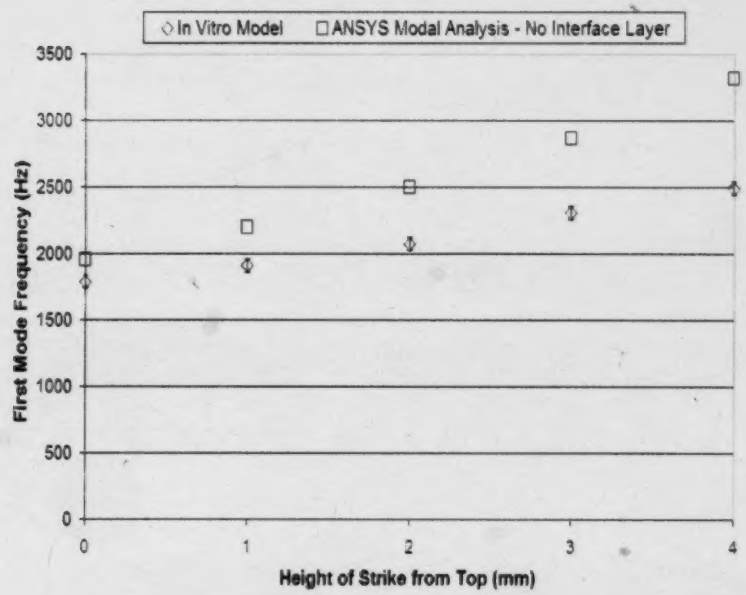

Figure 3.10: Comparison of Modal Analysis with No Interface Layer to *In Vitro* Model (First Mode)

The initial hypothesis was the modal analysis method itself. This method is akin to placing the structure on a shaker table and exciting the entire mass. The impact testing however imparts a small amount of energy to the system. It was hypothesized that this was insufficient to excite the entire mass of the disk. The strike would cause deflections in the disk in close proximity of the aluminium post, but the material at larger radii would not displace because there was insufficient energy to initiate motion. In this case, the resultant mass and stiffness matrices would be much smaller than those for the modal case, as the DOF's that weren't excited could be neglected. Thus, the two methods wouldn't be comparing the same systems. However, this cannot be true. Consider two nodes on either side of the limit of displacement in the disk. The node which moves will experience a shear stress where as the node which is stationary will not, according to Hook's Law. There will be a

discontinuity in the stress field at this location which is not possible in the finite element method. Thus the entire mass of the disk must be excited by the impacting rod so this cannot be the source of error.

The final explanation was that the error was caused by neglecting the acrylic interface layer. Although the interface layer is thin, the documented Young's modulus of acrylic is 1 - 3 GPa [47]. However, due to the inhomogeneity of the acrylic used *in vitro* (air bubbles, FRB particles, etc) the modulus was taken to be 0.5 GPa, which is an order of magnitude less than the modulus of the FRB disk. If the acrylic and FRB are thought of as two springs in series, the stiffness of the weaker spring is dominant, thus it is feasible that the interface layer could have a significant effect on the natural frequencies of the system even though the layer is thin compared to the disk. When the interface layer is included, with the properties found in Table 2.1, the model produced the results shown in Figure 3.11, using the code found in Appendix F, Section F.4. The error bars have equivalent meaning to the previous results.

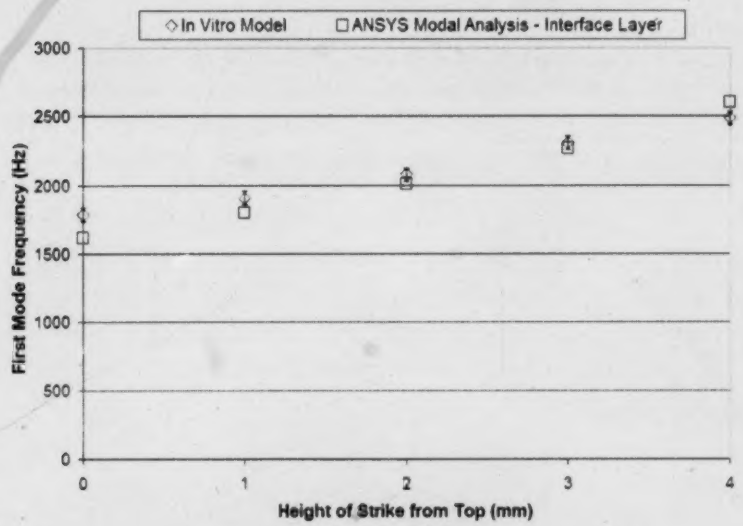

Figure 3.11: Comparison of Modal Analysis with Interface Layer to *In Vitro* Model

Although the response of the modal analysis with the interface layer still diverges from the *in vitro* response as striking height decreases, the results are more consistent than the previous model (5% error).

The second mode was more difficult to determine using modal analysis. Figure 3.12 depict the first ten mode shapes of the simulation. The second calculated mode involves axial vibrations of the aluminium post. Since the Periotest® accelerometer only measures accelerations in the radial plane this mode must be neglected when the modal results are compared to the *in vitro* results. Some of the other mode shapes contain localized oscillation of the point mass while the remainder of the model stays relatively stationary. It is believed this is due to ill-conditioning of the mass matrix since there are elements with relatively high density in close proximity to less dense elements. Therefore the accuracy of these modes is suspect.

The two modes shapes that do not vibrate axially and do not have predominant point mass oscillation are the fifth and sixth. Both of these mode shapes appear to be combinations of the predicted mode shapes shown in Figure 3.2. They both have resonant frequencies that are the same order of magnitude as the *in vitro* results (29 kHz for the fifth and 35kHz for the sixth). As such, it is difficult to decide which mode shape, if either, should be chosen as the "second mode shape". Due to these difficulties, second mode results are not presented for the modal analysis.

3.4.2 Simulating the *In Vitro* Model using Transient Analysis

The transient analysis model was constructed with the dimensions and properties listed in Table 2.1, including the interface layer. Figure 3.13 depicts the transient model consisting of approximately 15000 SOLID92 elements (1% convergence criterion). Again, only one half of the structure needed to be considered due to symmetry.

The method of exciting the structure in a transient analysis is important as the response of the structure will depend on the shape of the forcing function and the amount of time it is applied. As these factors are unknown for the *in vitro* situation, a transient forcing function could not be used. Instead, an impact between a simulated Periotest® rod and the aluminium post was used. To model the impact, contact elements were created between the two adjacent surfaces of the rod and post so that the impact rod and the rest of

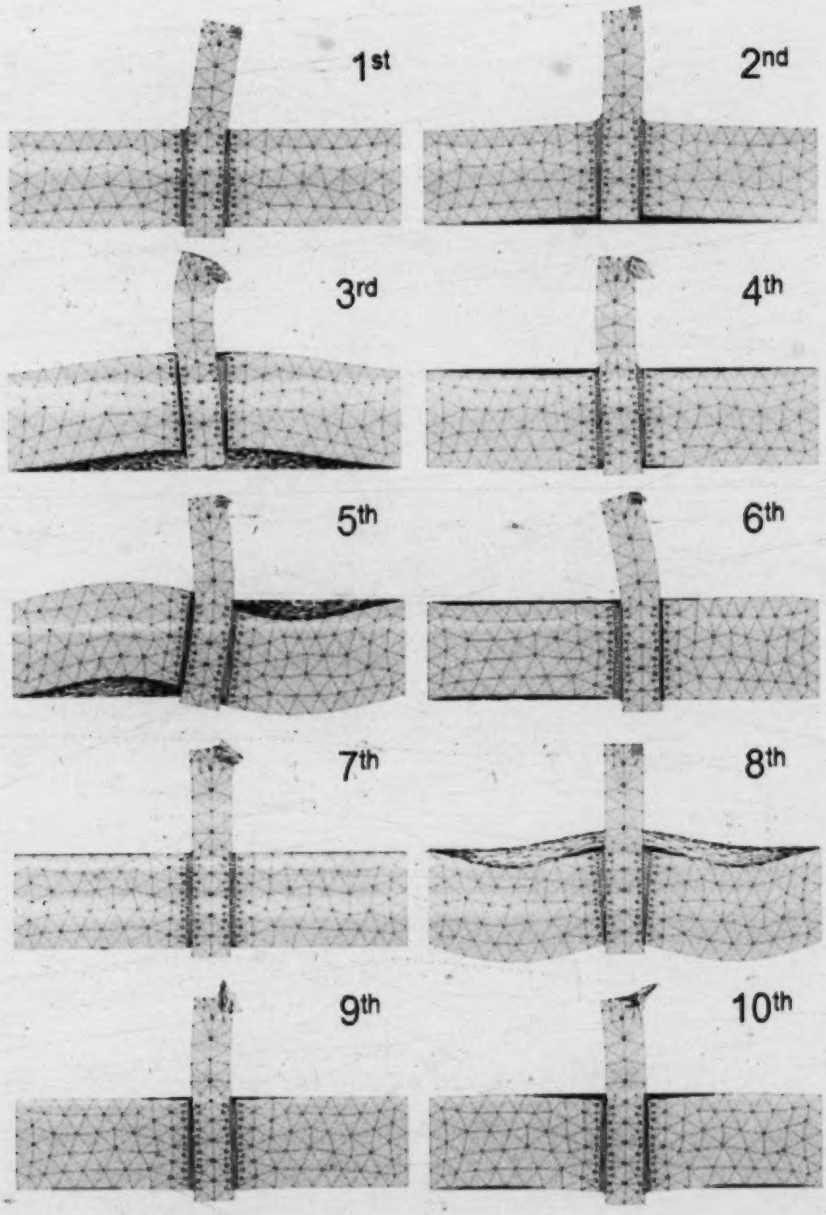

Figure 3.12: Mode Shapes for Modal Analysis (1-10)

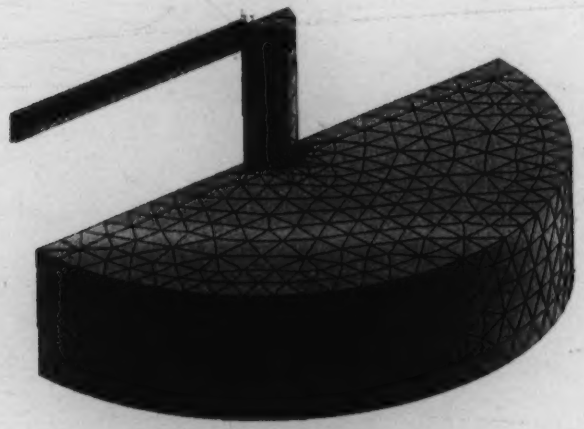

Figure 3.13: Transient Analysis Model

the system could move independently of each other without allowing the rod to penetrate the post. This was done using a combination of 3-D eight node, surface to surface contact elements which are used to represent contact and sliding between three dimensional deformable surfaces [48] (CONTA174) and 3-D target elements which overlay the solid elements describing the boundary of the deformable body [49] (TARGE170). Section 3.5 outlines how these elements function in the transient analysis.

The Periotest® rod was constrained to move horizontally and was assumed to have an initial velocity of 0.2 m/s to match the manufacturer's specifications of the Periotest's® performance. Since the impact of the rod is normal to the surface of the aluminium post, sliding is assumed to be negligible thus friction coefficients were ignored to save processing time. The transient analysis used a typical sampling rate of once every 0.6 microseconds. In cases where greater resolution was required this was increased such that the sampling rate was 20 times faster than the highest desired frequency, as recommended by ANSYS.

The transient simulation produced the results in Figures 3.14 and 3.15 at five striking heights. The lower frequency was determined by filtering out all frequencies above 5 kHz and then determining the contact time as

outlined in the introduction. The higher frequency was found using the custom MATLAB FFT software with all frequencies below 20 kHz filtered out. For Figure 3.14, the *in vitro* error bars again represent the resolution of the analysis of the Periotest® accelerometer signal. The transient analysis error bars represent the difference between to adjacent data points when calculating the contact time. For instance, there may not be a data point exactly on the zero displacement axis, thus it lies somewhere between the point before and after the axis crossing. For Figure 3.15, the *in vitro* and transient analysis error bars represent the frequency resolution of the FFT.

The first natural frequency results match well with the *in vitro* results with only a 3% relative error. There is a 13% error for the higher frequency, but the shape of the FEA results curve is qualitatively similar to the second mode *in vitro* results: Before the higher frequency was deemed to be a result of a higher mode being excited, further comparisons with analytical results were done.

3.4.2.1 Higher Frequency Investigation

Due to the difficulties encountered in determining the second mode during the modal analysis, further analytical results were used to verify the transient simulation produced the theoretically expected second natural frequency.

Although the FEA response signal (Figure 3.16) looks qualitatively similar to the accelerometer signal (Figure 1.3), the FEA signal is a plot of the displacement of a node from the aluminium post over time while the *in vitro* signal is an acceleration curve over time. A direct comparison between both the amplitude and time scales is therefore not possible. However, if the signals are assumed to be a combination of harmonic functions, the acceleration signal is equivalent to a sum of scaled displacement signals [40]. This scaling is independent of time however, therefore the frequencies evident in the displacement response are also evident in the acceleration response.

As both the experimental and numerical results have reasonably well correlated higher frequency components, the higher frequency does not appear to be due to electronic or numerical "noise". In addition the contact status of the impacting rod and the aluminium post remained closed throughout the entire time, suggesting that the higher frequency did not originate from "bouncing" of the impact rod. Thus it is likely that this higher frequency is the second natural frequency of the system.

To verify if the transient analysis model can produce accurate second

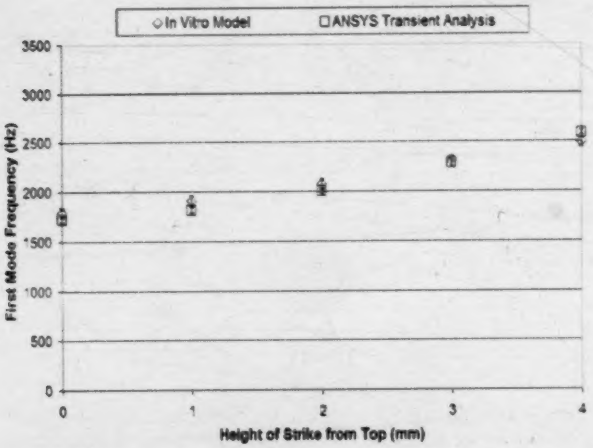

Figure 3.14: Comparison of Transient Analysis to *In Vitro* Model

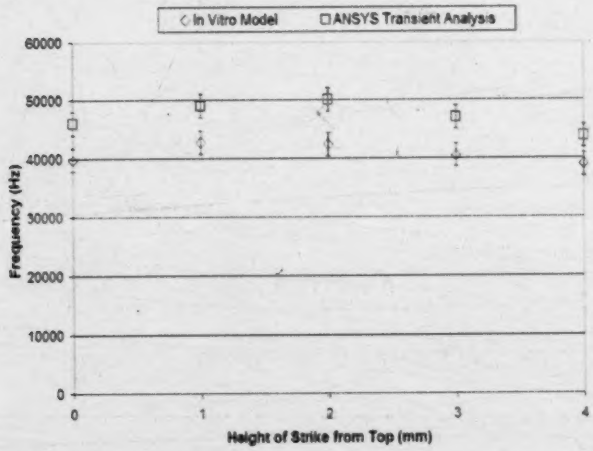

Figure 3.15: Comparison of Higher Frequency from Transient Analysis to *In Vitro* Model

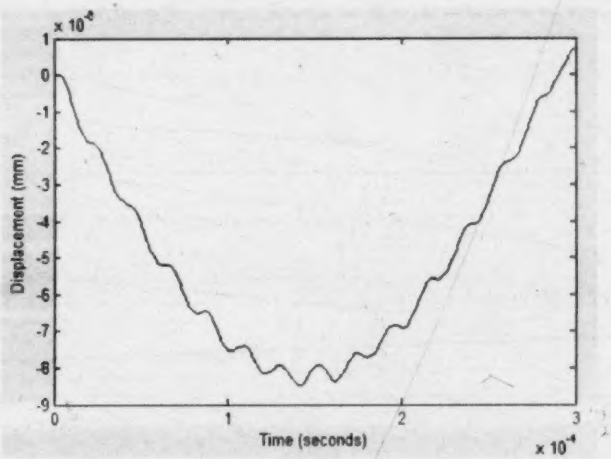

Figure 3.16: Typical Transient Analysis Signal

mode frequencies, the *in vitro* system, while being impacted with the rod at the free end, was modelled as a Bernoulli-Euler beam fixed at one end with a point mass at the other [42] and compared to the transient results. The solution for this problem results in the transcendental equation for the frequency parameter (βL) given in Appendix E. For the beam parameters given in Table 2.1, the first two values of (βL) are 0.5776 and 3.9311. The theoretical natural frequency of vibration of this system can be determined using Equation (3.1).

The transient model was used to determine the first and second natural frequencies of a system with an infinitely stiff disk and interface layer resulting in a rigidly fixed, 10 mm long cantilevered aluminium post similar to the Bernoulli-Euler approximation. All other geometry, material properties and boundary conditions remained the same as the transient verification model. The FEA results were compared to the frequencies predicted by Equation (3.1) in Table 3.8.

The FEA model was within 0.8% relative error of the analytical solution for both cases. As this is below the convergence criterion of 1%, the model yielded acceptable results.

Since no separation was found to occur during the strike in the finite

Table 3.8: First and Second Natural Frequency Comparison for Cantilevered Aluminium Post

Method	First Natural Frequency (Hz)	Second Natural Frequency (kHz)
Analytical	2711	126
FEA	2728	127

element analysis and the model predicted the second natural frequency for both the analytical and *in vitro* cases, there is strong evidence that the higher frequency in the experimental signal is indeed a second mode of vibration of the implant-abutment system.

3.4.2.2 Sensitivity of Transient Analysis to Defining Variables

Since the second natural frequency curve of the transient results seems qualitatively similar to the *in vitro* results (Figure 3.15), but shifted up by approximately 5kHz, a sensitivity investigation was undertaken on the transient model to determine if slight alterations of the material properties or dimensions of the model produced more closely matched results for the second natural frequency while not increasing the relative error of the first.

Figures 3.17 to 3.21 outline the results of this sensitivity study. Second order polynomial best fit curves have been included to help display the results but are not meant to be interpolations between data points. Dimensions such as disk radius and thickness, post radius and length, and impact rod radius and length were not altered since they could be accurately measured. Other material properties, such as Young's modulus of the impact rod and disk, and density of the disk and interface layer were found to have a negligible effect on the first and second natural frequencies of the system and thus were not included.

As shown in the figures, the only variable that could be altered to decrease the second natural frequency while maintaining the first is the density of the aluminium post. Varying the density from 2500 kg/m^3 to 3100 kg/m^3 only varied first mode by 50 Hz while second mode dropped from 50 kHz to 45 kHz. However, the density would have to be approximately doubled to produce the desired results and measurements of the *in vitro* post prove this to be

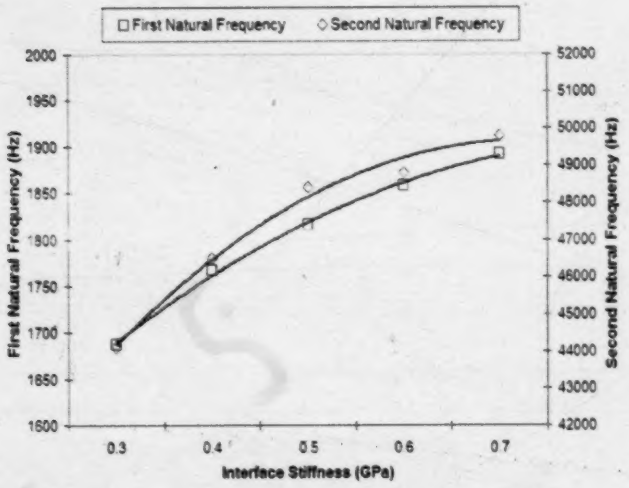

Figure 3.17: Sensitivity Results for Altering Interface Young's Modulus

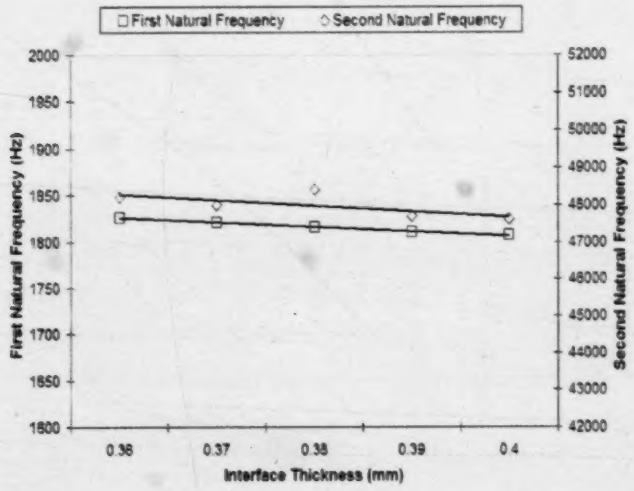

Figure 3.18: Sensitivity Results for Altering Interface Thickness

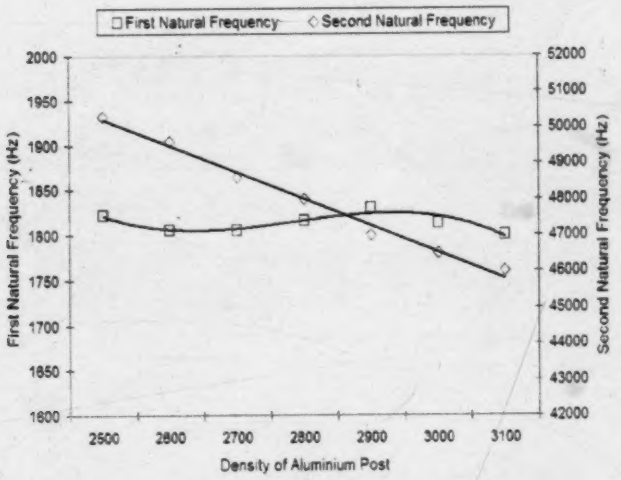

Figure 3.19: Sensitivity Results for Altering Aluminium Post Density

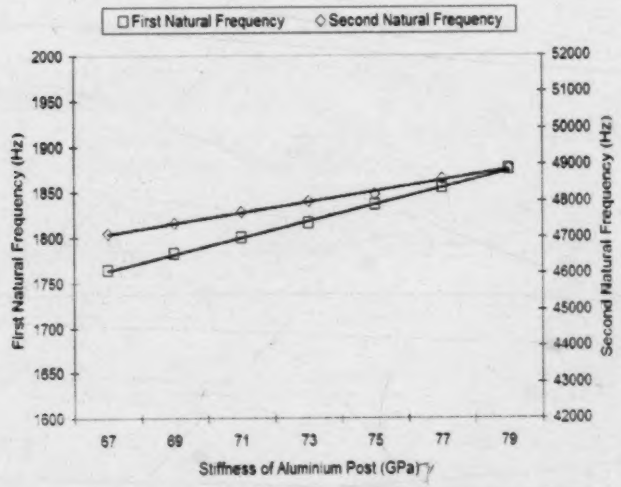

Figure 3.20: Sensitivity Results for Altering Aluminium Post Young's Modulus

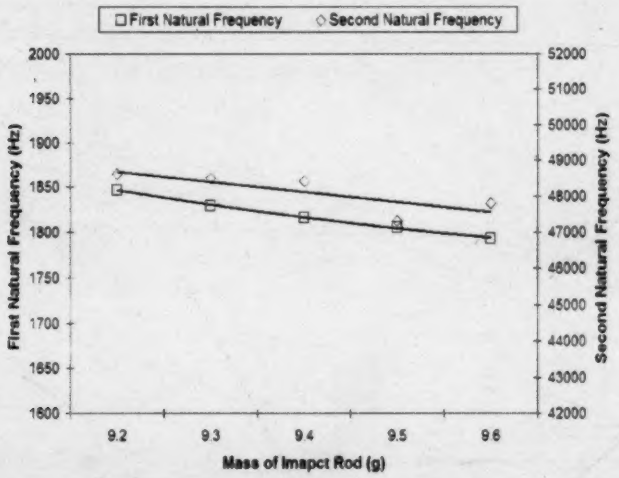

Figure 3.21: Sensitivity Results for Altering Mass of Impact Rod

unrealistic. Thus the results in Figures 3.14 and 3.15 seem to be the most appropriate values.

3.4.3 Choosing the "Better" Model

Consider the criterion for choosing the "better" model. The processing time for the transient analysis was much longer than the modal analysis: approximately 6 hours compared to 30 minutes. However, the relative error for the first mode of the transient solution was only 3% compared to 5% for the modal analysis. In addition, the transient analysis method, unlike modal analysis, can include contact elements which are appropriate for simulating a loss of osseointegration. Finally, as shown in Figure 3.15, the transient solution produced reasonable second mode frequencies while the modal analysis results for the higher mode shapes were difficult to evaluate. Therefore the transient analysis model was deemed the better model.

3.5 The Use of Contact Elements in the Transient Analysis

The combination of contact and target elements is used to represent contact and sliding between 3-D surfaces. The elements are located on the surface of existing 3-D solid elements with midside nodes, sharing the same geometric characteristics as the solid to which it is connected. It is stated in the element description that "contact occurs when the element surface penetrates one of the target segment elements on a specified target surface." [48] Although this seems straight forward, the processes of determining if contact has occurred and the result thereafter are somewhat complex and will be discussed briefly below.

3.5.1 Contact Status and Pinball Radius

According to the ANSYS Structural Guide [50], "the position and the motion of a contact element relative to its associated target surface determines the contact element status". The contact status can be one of four options:

Open far-field contact	Sliding contact
Open near-field contact	Sticking contact

The two possibilities of interest here are open far and near-field contact. Open far-field contact refers to a case when the contact and target elements are reasonably far from each other and the possibility that contact will occur in the next time step is unlikely. Contact element solutions are solved iteratively thus the choice of transient solution options, such as time step intervals, are important for a convergent solution. This will be further discussed in Section 3.5.2. Open near-field contact refers to the case when the contact and target elements are close to each other and contact will likely occur in the next time step.

The target elements monitor contact status at Gauss points, calculated positions between the nodes of the element as determined by the Gauss integration procedure [51]. Imagine a sphere around each of these Gauss points, whose radius is called the pinball radius, depicted in Figure 3.22. If a Gauss point of a contact element enters this sphere the status changes from far to

near-field contact. The pinball radius defaults to four times the depth of the underlying element but can be changed if deemed necessary.

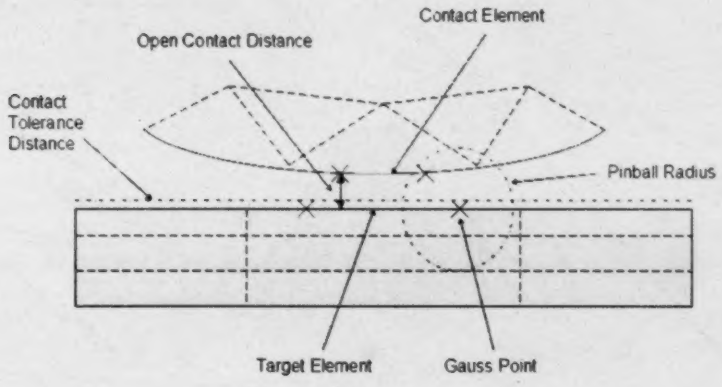

Figure 3.22: Surface to Surface Contact Depiction

3.5.2 Importance of Time Step Intervals

Time step intervals are a very important factor concerning contact status. If the time step interval is large it will require fewer steps to reach the final time value, thus the solution will be found in a shorter period of time. However, if the interval is too large it is possible that at time t the contact element is outside the pinball radius and at time $t + \Delta t$ the contact element has passed through the pinball region and out the other side, again falling outside the pinball radius. Since contact status is only updated at the end of each time step interval the status would remain as open far-field contact. In this case the solution is still found, however it will be equivalent to the case where contact elements were not included and thus be erroneous.

If the time step intervals are small, the above problem will not occur, but it will take a great deal of time for the status to change to open near-field contact. Generally nothing of importance to the analysis occurs while the contact status is open far-field contact thus this is wasted processing time.

It is therefore beneficial to optimize the time step interval to minimize processing time and yet still converge to an accurate solution. Once open near-field contact status has been reached, a key-option in the CONTA174 element description can be implemented which begins to decrease the time step interval. This way a relatively large time step interval can be used to minimize the amount of processing required to reach open near-field contact and then it is reduced to improve convergence when contact is imminent.

3.5.3 Importance of Element Size

Once open near-field contact status has been reached the distance from the contact element Gauss point to a surface joining the target element Gauss points is calculated until it is less than a prescribed tolerance, as shown in Figure 3.22. At this point the elements are said to be in contact. This is done for all contact/target possibilities thus it is beneficial to use as few elements as possible to minimize processing time. However, if the elements are too large this generally causes convergence or contact status problems. So again an optimization of contact and target element size must be found.

3.5.4 Contact Algorithms

Once contact has been established, the status will change to either sliding or sticking contact. This will depend on parameters selected by the user according to the required information. The intricacies of both sliding and sticking contact were deemed unnecessary here, thus the general algorithm to enforce contact used in both will be covered. There is a choice of two contact algorithms: penalty method and augmented Lagrangian method (ALM).

In order to illustrate the penalty method through an example, consider the problem depicted in Figure 3.23. This cantilevered beam can be described using finite element theory as follows, considering only the deflections (rotational DOF's not shown for clarity).

$$\begin{bmatrix} k_{11} & k_{22} & k_{33} \\ k_{21} & k_{22} & k_{23} \\ k_{31} & k_{32} & k_{33} \end{bmatrix} \begin{pmatrix} u_1 \\ u_2 \\ u_3 \end{pmatrix} = \begin{pmatrix} F_1 \\ F_2 \\ F_3 \end{pmatrix} \tag{3.3}$$

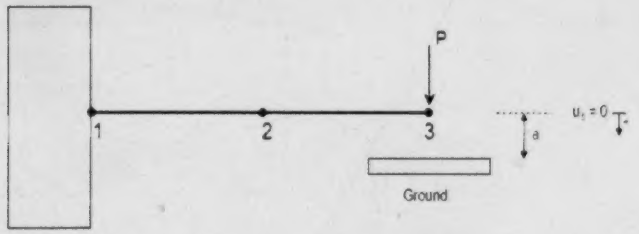

Figure 3.23: Cantilever Beam Meshed with Two Elements

Considering the loading conditions, we can rewrite equation (3.3) as:

$$\begin{bmatrix} k_{11} & k_{22} & k_{33} \\ k_{21} & k_{22} & k_{23} \\ k_{31} & k_{32} & k_{33} \end{bmatrix} \begin{pmatrix} u_1 \\ u_2 \\ u_3 \end{pmatrix} = \begin{pmatrix} 0 \\ 0 \\ P \end{pmatrix} \tag{3.4}$$

If P is large enough, the beam will bend down until it touches the ground, at a deflection $u_3 = a$. According to the finite element expression, there is nothing to say that "ground" exists, thus the beam would continue to bend. However, if a contact element were present, the tip of the beam would have entered the pinball radius of the target element on the ground, changing the status to open near-field contact. The first time step in which the tip has passed the plane at a the penalty method would be implemented.

The penalty method uses a large penalty constant (C), relative to the entries in the stiffness matrix, to basically swamp out other terms in the equation and form a constraint on the system. For problems involving bending ANSYS recommends using $C = 0.1 \cdot max|E|$ without concern for the discrepancy in units. The ANSYS Structural Guide [50] states this recommendation satisfies the suggested value $C = max|K_{ij}| \times 10^4$ in most cases without having to calculate the maximum K_{ij} value, which saves processing time [52].

For the example above, the third node cannot pass through a thus its displacement, u_3, must be constrained to equal a. This is done by adding C to the node's diagonal term in the stiffness matrix, k_{33}, and adding $(C \cdot a)$ to the node's term in the force matrix (P).

$$\begin{bmatrix} k_{11} & k_{12} & k_{13} \\ k_{21} & k_{22} & k_{23} \\ k_{31} & k_{32} & (k_{33}+C) \end{bmatrix} \begin{pmatrix} u_1 \\ u_2 \\ u_3 \end{pmatrix} = \begin{pmatrix} 0 \\ 0 \\ (P+Ca) \end{pmatrix} \tag{3.5}$$

Expanding the final equation in the set:

$$k_{31} \cdot u_1 + k_{32} \cdot u_2 + (k_{33}+C) \cdot u_3 = (P+Ca) \tag{3.6}$$

and dividing by C:

$$\frac{k_{31}}{C}u_1 + \frac{k_{32}}{C}u_2 + (\frac{k_{33}}{C}+1)u_3 = (\frac{P}{C}+a) \tag{3.7}$$

From Equation (3.7) it is apparent that if C satisfies the recommendation above, and noting that $\frac{P}{C}$ is generally of small magnitude, the equation is approximately equal to:

$$u_3 \simeq a \tag{3.8}$$

which is the desired constraint on the system. This can be changed slightly so that the vertical location of u_3 could be constrained to the vertical location of a node on a surface below it. Thus if the surface moved so would the tip of the beam. The forces generated between the nodes in contact must be checked at the end of every iteration to ensure that they remain in compression. If the forces become tensile then the penalty constant must be removed because the nodes are losing contact and should no longer be constrained.

This method has some distinct advantages: it is relatively simple to implement, it introduces no new equations and has a physical interpretation. However, the penalty method suffers from ill-conditioning that worsens as the penalty constant is increased, while constraints are satisfied exactly only in the limit of infinite penalty values [53].

A basic explanation as to why the penalty method can suffer from ill-conditioning is as follows. If the penalty constant is very large, it is like introducing a very stiff spring into the system. Since the penalty method is only implemented during the time step after the contact Gauss point has passed through the target element this new spring is under compression. Before the solver moves onto the next time step it iterates to find the equilibrium position of this new system, which includes the spring. To do this, the contact element is "pushed back" as the spring settles at equilibrium, where the contact Gauss point lies on the surface of the target element (or within a prescribed tolerance value). However, if the spring is too stiff, it

pushes the contact element out of the pinball radius and thus the contact status changes to open far-field contact. The solver deems this acceptable and moves onto the next time step and the solution attempt fails.

However, as stated above, the constraint is only satisfied exactly as C approaches infinity, as shown in Equations (3.7) and (3.8). Using a finite value of C inevitably introduces numerical error. It is therefore beneficial to use the ALM to increase the accuracy of the solution.

Unfortunately, the Augmented Lagrangian Method does not lend itself to physical interpretation. It is merely a complex set of equations utilizing concepts from the energy method, Lagrange multipliers and the penalty method. Full descriptions on this derivation or its implementation can be found in [53], [54] and [55]. In short, the solution is found by solving a complex integral containing the Lagrange multiplier and a penalty term such that it satisfies the constraint condition.

It may seem that this method would require more processing time to solve these complex integrals, which would be true if only one iteration were required. However, the ALM will converge to a solution much faster than the penalty method, and with greater accuracy. It is also not prone to the ill-conditioning which plagues the penalty method. Therefore, for complex systems, such as the one in question, the ALM will greatly reduce processing time while increasing accuracy over the penalty approach. This is the reason it was used for this application.

Chapter 4

FEA Simulation Results

As described in the introduction, a healthy implant will begin the osseointegration process almost immediately after implantation. Ideally, the host bone will create a strong, lasting interface with the implant. Unfortunately, this is not always the case. The osseointegration process can fail, the bone around the neck of the implant can begin to recede or a layer of connective soft tissue can form around the implant. Since all of these possibilities create a change in the bone or interface surrounding the implant, there should be a measurable change in the impact test signal. Indeed, according to patient data, there is a drop in the first natural frequency before an implant fails. The goal in this chapter is to quantitatively simulate the changes in frequency for each of these failure situations and use this information to predict the source of the *in vivo* failures so preventative measures can be taken.

Some of these situations are difficult to simulate with *in vitro* experiments. A reduction in bone margin height may be possible, but a loss of osseointegration would be difficult to simulate. For these situations the FEA approach provides an excellent alternative. Having shown the FEA simulation to produce realistic results compared to the *in vitro* model for the first and second natural frequencies, the simulations are altered to simulate these degenerative situations.

4.1 Simulating the Changes in the Interface Layer

The three specific changes in the implant - bone interface which are simulated are loss of osseointegration, loss of bone margin height and development of connective soft tissue in the bone-implant interface. This was accomplished through modifications to the interface region of the model. Full osseointegration is simulated in the FEA model by having the aluminium post and interface layer share nodes along their common boundaries, thus allowing no separation between the two. When a loss of osseointegration is simulated, the post and interface layer no longer share nodes along the common boundaries. Instead a layer of contact elements are meshed between the two to allow separation, but not penetration, in the area of osseointegration loss. The nodes below this loss still coincide however. For the simulation of reduced bone margin height, the height of the interface layer is reduced to simulate receding bone around the neck of the implant. From a mechanical viewpoint, the difference in these two cases is that while there is no possibility of generating tensile forces between the post and the surrounding interface layer in either case, compressive forces can be generated in the situation in which there is only a loss of osseointegration. The development of connective soft tissue in the interface layer is simply modelled as a reduction in the stiffness of the entire interface layer.

The simulations are for the typical implant-abutment systems mentioned previously (extraoral prostheses: 4 mm implants with 5 mm abutments and oral implants: 9 mm implants with 10 mm abutments). In all instances it was assumed that the rod impacts the top of the abutment. In the extraoral case, the dimensions of the model were altered from those found in Table 2.1 to those found in Table 4.1 and depicted in Figure 4.1. Again the outer cylindrical surface of the disk was constrained and the mesh size was reduced, specifically around the interface layer, until 1% convergence was reached. Sample code for constructing these models can be found in Appendix F, Section F.5.

4.1.1 Results of Changes in the Interface Layer

Figures 4.2 to 4.5 show the variation in the values of the first and second natural frequencies that occur for the simulated increasing loss of osseoin-

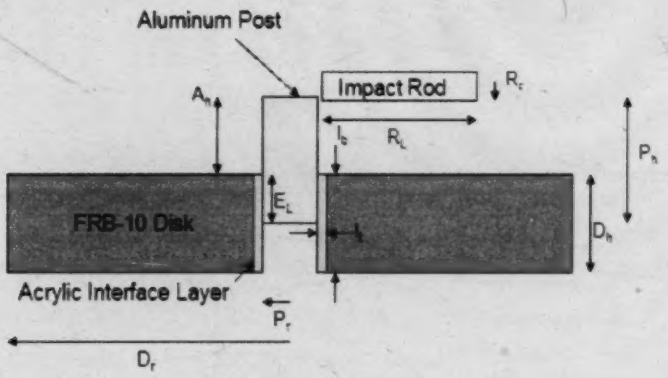

Figure 4.1: Schematic of Simplified BAHA Model

tegration and loss of bone margin height for oral implants (Figures 4.2 and 4.3) and the extra-oral (BAHA) implants (Figures 4.4 and 4.5). It has been assumed that the region of loss begins at the outer surface (skin side) of the hard tissue and propagates towards the base of the implant [56]. The error bars for the first natural frequency plots represent the contact time error described in Section 3.4.2 while those for the second natural frequency plots represent the FFT resolution.

For the first (lowest) natural frequency (Figures 4.2 and 4.4), both sizes

Table 4.1: Model Properties for Extraoral Prostheses (BAHA)

Post Radius (P_r)	2 mm	Post Height (P_h)	20 mm
Abutment Height (A_h)	5 mm	Engagement Length (E_L)	4 mm
Interface Thickness (I_t)	0.38 mm	Interface Height (I_h)	9 mm
Disk Radius (D_r)	20 mm	Disk Height (D_h)	9 mm
Periotest® Rod Radius (R_r)	1 mm	Periotest® Rod Length (R_L)	20 mm

of implant-abutments evaluated show measurable changes for relatively small regions of loss. As it has been reported that changes equivalent to 100 Hz are statistically significant [21], a loss of approximately 0.2 mm would be detectable for the shorter implants and 0.4 mm for the longer system. The difference in loss (osseointegration vs. bone loss) is not distinguishable until the loss has extended to approximately 0.8 mm for the shorter implant and to approximately 1.9 mm for the longer, down the height of the implant, depicted as "h" in Figures 4.2 to 4.5. While the second (higher) natural frequencies (Figures 4.3 and 4.5) show a similar trend as the length of the loss zone increases, the differences between loss of osseointegration and bone loss are not as evident.

The simulations for the development of a softer interface layer, which could correspond to the development of connective soft tissue or reduced stiffness during healing, are given in Figures 4.6 to 4.9 for the two sizes of implants. The error bars have equivalent meaning to the previous figures. Figures 4.6 and 4.8 show the dramatic change in the lowest natural frequency as the stiffness (modulus of elasticity) of the interface layer changes. The region between the dashed lines is an estimated range of modulus of elasticity for soft connective tissue (scar tissue) to hard tissue (quality bone) and it is evident that the lowest natural frequency can change in the order of 50% and therefore would be easily detectable. The higher natural frequency also shows a similar percentage change with stiffness, however, the actual change in frequency is even larger than for the lower natural frequency. It should be remembered that for these simulations, the change in stiffness occurs over the entire interface simultaneously.

Examining Figures 4.3 and 4.5, there appears to be large, sudden drops in the second frequency as the amount of loss, be it osseointegration or bone margin height, occurs. For the oral case (Figure 4.3) this occurs between 2 and 3 mm of bone loss, while for the BAHA (Figure 4.5) it occurs between 1 and 1.5 mm for both a loss in osseointegration and bone margin height. This is intriguing and the source of this phenomena is unknown. A speculative explanation would draw from the problems experienced when looking for the second mode using modal analysis. Even if the modes that have localized oscillation of the point mass are neglected, there are still a number of mode shapes that seem reasonable and have frequencies in the same order of magnitude. It is hypothesized that as the amount of loss increases, there is a point were the dominant second mode shape switches from one shape to another. This is supported by the FFT output shown in Figures 4.10 and 4.11. The

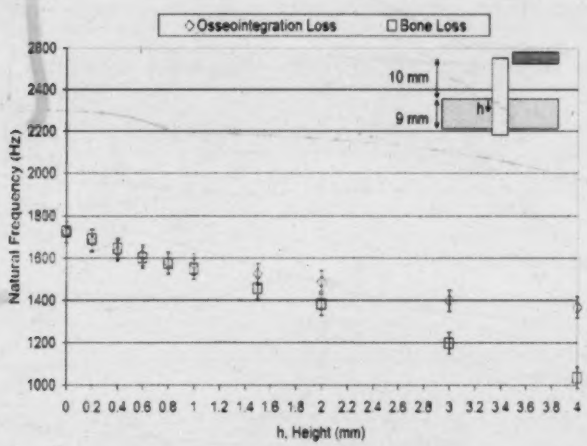

Figure 4.2: First Natural Frequency Comparison for Simulated Loss of Osseointegration and Loss of Bone Margin Height (Oral Implants)

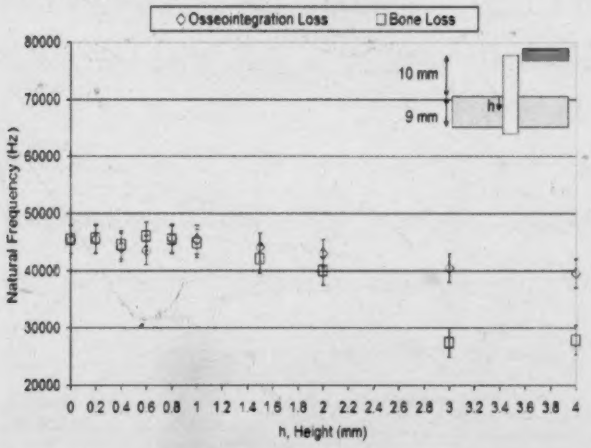

Figure 4.3: Second Natural Frequency Comparison for Simulated Loss of Osseointegration and Loss of Bone Margin Height (Oral Implants)

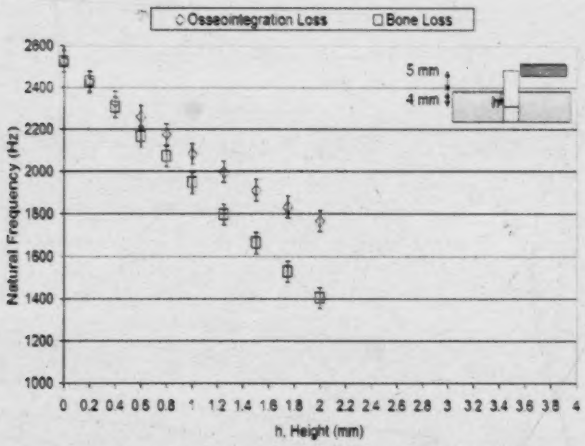

Figure 4.4: First Natural Frequency Comparison for Simulated Loss of Osseointegration and Loss of Bone Margin Height (BAHA Implants)

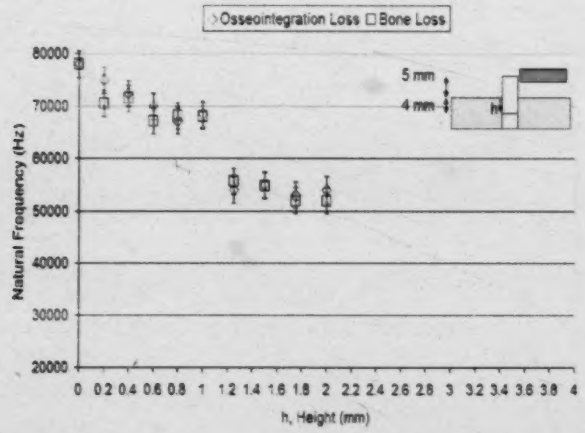

Figure 4.5: Second Natural Frequency Comparison for Simulated Loss of Osseointegration and Loss of Bone Margin Height (BAHA Implants)

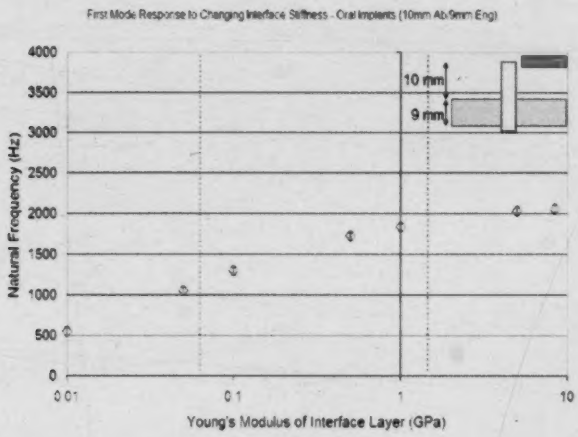

Figure 4.6: First Mode Response to Changing Interface Stiffness - Oral Implant

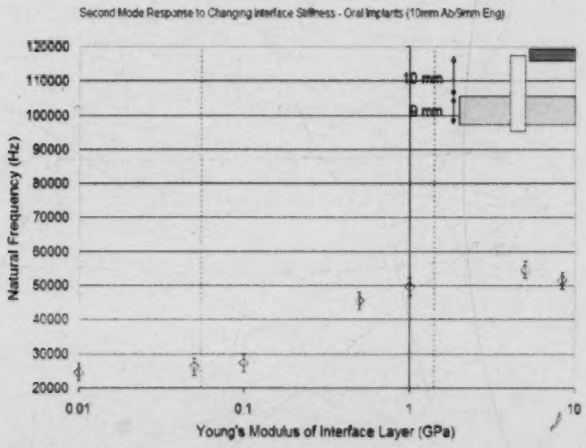

Figure 4.7: Second Mode Response to Changing Interface Stiffness - Oral Implant

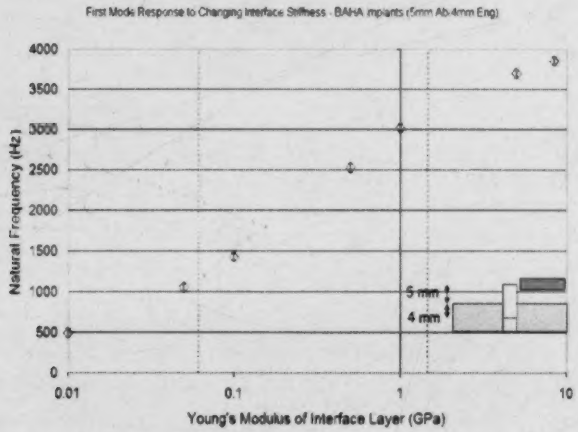

Figure 4.8: First Mode Response to Changing Interface Stiffness - BAHA Implant

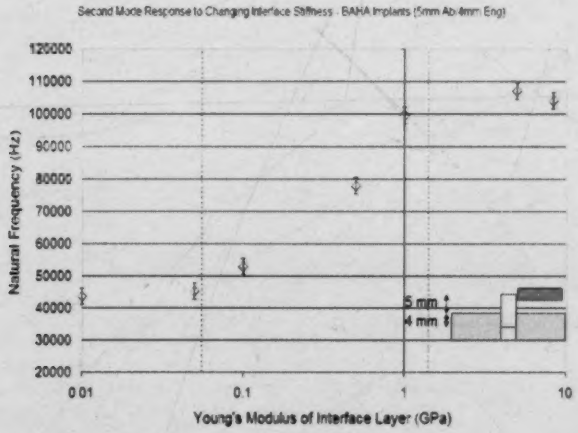

Figure 4.9: Second Mode Response to Changing Interface Stiffness - BAHA Implant

dominant spike in Figure 4.10 occurs around 68kHz, but there is a lesser spike around 55kHz. Although the signal is quite noisy, this could be interpreted as two modes being excited where the modal participation factor of the mode with a resonant frequency of 68kHz is greater than the other. In Figure 4.10, the changing constraint conditions on the aluminium post no longer support the original mode shape (bending for example) thus the MPF of that mode decreases and the mode present at 55kHz dominates (translational perhaps). This could be valuable information when interpreting *in vivo* results. If there appears to be a large drop in the second natural frequency it could be due to a change in dominant second mode, thus signalling a possible failure of the implant.

When the first and second natural frequency data are used in conjunction it shows promise for determining the cause of frequency changes *in vivo*. For instance, consider a BAHA patient. If the first natural frequency drops from 2500 Hz to 2000 Hz it could be due to a change in stiffness of the interface layer due to remodelling of the bone, which may be beneficial to the integrity of the implant. However, it could be a loss of bone margin height and preventative measures should be started to attempt to save the implant. If the second natural frequency was found to drop from around 80 kHz to 60 kHz however, it could be estimated from Figures 4.4, 4.5, 4.8 and 4.9 that this could only be due to a change in stiffness of the interface layer. The drop in second natural frequency is too large to be a loss of bone margin height. Using this comparative analysis technique may allow more accurate prediction of the cause of changes in natural frequency.

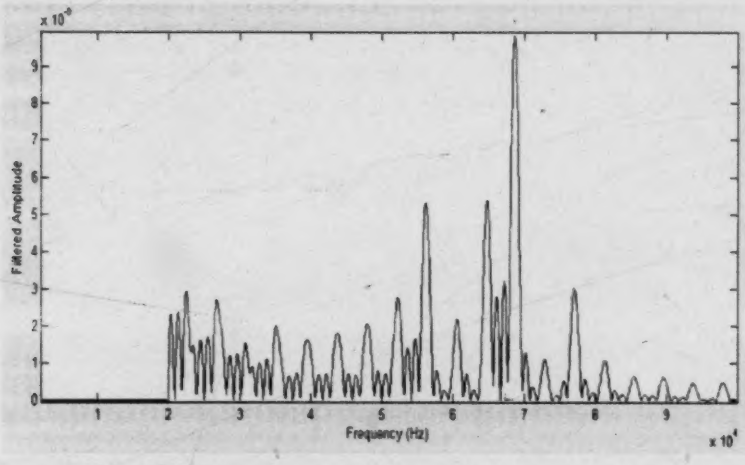

Figure 4.10: Filtered FFT Output for A Simulated Impact Test on BAHA Model with 1mm of Osseointegration Loss

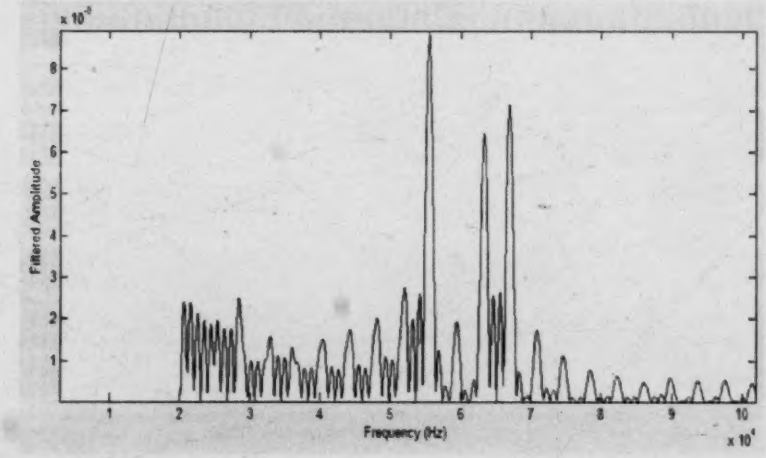

Figure 4.11: Filtered FFT Output for A Simulated Impact Test on BAHA Model with 1.5mm of Osseointegration Loss

Chapter 5

Conclusions

With the development of impact testing it appears to be possible to quantitatively measure changes in implant status *in vivo* by monitoring the natural frequency of the implant - tissue system. However, due to the constant remodelling at the interface it is difficult to determine the source of these changes. Thus, the *in vitro* model was developed and shown to produce similar results to the *in vivo* situation while enabling strict control over the dominant variables affecting the response of the system. In order to expand the study further and obtain quantitative data for various simulated failure modes, a finite element simulation of the *in vitro* model was developed. This model had a distinct interface region rather than one with the implant directly coupled to the hard tissue. This allowed the introduction of different interface stiffnesses as well as introducing contact elements to simulate a loss of osseointegration. This interface model was verified through comparison to *in vitro* experiment and analytical analysis and used to answer three important questions regarding impact testing of implants.

Firstly, the higher frequency visible on the raw accelerometer signal is not due to bouncing of the impact rod against the implant. The contact status remained closed during simulations at all striking heights. Due to the strong correlation between this higher frequency and the simulated second mode, it appears it is in fact a second natural frequency of the system.

Secondly, the results of the FEA simulation indicate that clinical changes in the integrity of the interface (loss of osseointegration, loss of bone margin height, development of connective soft tissue) should be detectable from the frequency response changes. The simulations indicate that with either a loss of osseointegration or bone margin height for the shorter implant of as little

as 0.2 mm, the change in frequency response is sufficient to be clinically detectable. In addition, changes in the stiffness of the interface, such as might occur after initial implant placement or through the development of connective soft tissue, result in easily measurable frequency changes. These changes are so minor, however, that it is unlikely they could be detected using conventional diagnostic techniques.

Finally, the potential of using the additional information provided by the second (higher) natural frequency is promising and could prove to be valuable. When used in conjunction with the lower natural frequency it is possible to predict the source of changes in the interface stiffness. However, the precision of the second natural frequency is still a concern since it required an FFT to determine the frequency from the displacement data.

References

[1] P.I. Branemark, G. Zarb, and T. Albrektsson. *Tissue-Integrated Prostheses: Osseointegration in Clinical Dentistry*. Quintessence Publishing Co., 1985.

[2] R. Adell, U. Lekholm, B. Rockler, and P.I. Branemark. A 15-year study of osseointegrated implants in the treatment of edentulous jaw. *International Journal of Oral Surgery*, 6:387–416, 1981.

[3] T. Albrektsson, G. Zarb, P. Worthington, and A.R. Eriksson. The long-term efficacy of currently used dental implants. a review and proposed criteria for success. *International Journal of Oral and Maxillofacial Implants*, 1(1):11–25, 1986.

[4] S. Sundén, K. Gröndahl, and H.-G. Gröndahl. Accuracy and precision in the radiographic diagnosis of clinical instability in brånemark dental implants. *Clinical Oral Implants Research*, 6:220–226, 1995.

[5] J. Elias, J. Brunski, and H. Scarton. A dynamic modal testing technique for noninvasive assessment of bone-dental implant interfaces. *International Journal of Oral and Maxillofacial Implants*, 11(6):728–734, 1996.

[6] L. Carlsson, T. Röstlund, B. Albrektsson, and T. Albrektsson. Removal torques for polished and rough titanium implants. *International Journal of Oral and Maxillofacial Implants*, 3(1):21–24, 1988.

[7] J. Duyck, H. J. Rønold, H. van Oosterwyck, I. Naert, J. Vander Sloten, and J. E. Ellingsen. The influence of static and dynamic loading on marginal bone reactions around osseointegrated implants: an animal experimental study. *Clinical Oral Implants Research*, 12:207–218, 2001.

[8] N. Meredith, K. Book, B. Friberg, T. Jemt, and L. Sennerby. Resonance

frequency measurements of implant stability *in vivo*. *Clinical Oral Implants Research*, 8:226–233, 1997.

[9] N. Meredith, D. Alleyne, and P. Cawley. Quantitative determination of the stability of the implant-tissue interface using resonance frequency analysis. *Clinical Oral Implants Research*, 7:261–267, 1996.

[10] R. Nedir, M. Bischof, S. Szmukler-Moncler, J.P. Bernard, and Jacky Samson. Predicting osseointegration by means of implant primary stability. *Clinical Oral Implants Research*, 15:520–528, 2004.

[11] M. Bischof, R. Nedir, S. Szmukler-Moncler, J.P. Bernard, and Jacky Samson. Implant stability measurement of delayed and immediately loaded implants during healing. *Clinical Oral Implants Research*, 15:529–539, 2004.

[12] R. Glauser, L. Sennerby, N. Meredith, A. Rée, A. Lundgren, J. Gottlow, and C. Hämmerle. Resonance frequency analysis of implants subjected to immediate or early function occlusal loading. *Clinical Oral Implants Research*, 15:428–434, 2004.

[13] Neil Meredith. *On The Clinical Measurement of Implant Stability and Osseointegration*. PhD thesis, Department of Biomaterials/Handicap Research, Institute for Surgical Sciences, Göteborg University, Göteborg, Sweden, 1997.

[14] H.-M. Huang, C.-L. Chiu, C.-Y. Yeh, C.-T. Lin, L.-H. Lin, and S.-Y. Lee. Early detection of implant healing process using resonance frequency analysis. *Clinical Oral Implants Research*, 14:437–443, 2003.

[15] D. Lukas and W. Schulte. Periotest - a dynamic procedure for the diagnosis of the human periodontium. *Clinical Physics and Physiological Measurement*, 11:65–75, 1990.

[16] W. Schulte and D. Lukas. Periotest to monitor osseointegration and to check the occlusion in oral implantology. *Journal of Oral Implantology*, 19:23–32, 1993.

[17] G. Faulkner, J. Wolfaardt, and A. Chan. Measuring abutment/implant joint integrity with the periotest instrument. *International Journal of Oral and Maxillofacial Implants*, 14(5):681–688, 1999.

[18] D. van Steenberghe, J. Tricio, I. Naert, and M. Nys. Damping characteristics of bone-to-implant interfaces; a clinical study with the periotest device. *Clinical Oral Implants Research*, 6:31–39, 1995.

[19] J. Olivé and C. Aparicio. The periotest method as a measure of osseointegrated oral implant stability. *International Journal of Oral and Maxillofacial Implants*, 5(4):390–400, 1990.

[20] A.B. Carr, E. Papzoglou, and P. Larsen. The relationship of periotest values, biomaterials, and torque to failure in adult baboons. *International Journal of Prosthodontics*, 8:15–20, 1995.

[21] G. Faulkner, D. Giannitsios, W. Lipsett, and J. Wolfaardt. The use and abuse of the periotest for 2-piece implant/abutment systems. *International Journal of Oral and Maxillofacial Implants*, 16(4):486–494, 2001.

[22] James Earthman. System and method for quantitative measurements of energy damping capacity. United States Patent, September 19, 2000. Patent Number - 6,120,466.

[23] B. Dejak, A. Mlotkowski, and M. Romanowicz. Finite element analysis of stresses in molars during clenching and mastication. *The Journal of Prosthetic Dentistry*, 90(6):591–597, 2003.

[24] L. Jimmlová, T. Dostálová, A. Kácovský, and S. Konvičková. Influence of implant length and diameter on stress distribution: A finite element analysis. *Journal of Prosthetic Dentistry*, 91(1):20–25, 2004.

[25] S. Ishigaki, T. Nakano, S. Yamada, T. Nakamura, and F. Takashima. Biomechanical stress in bone surrounding an implant under simulated chewing. *Clinical Oral Implants Research*, 14:97–102, 2003.

[26] A. O'Mahony, J. Williams, and P. Spencer. Anisotropic elasticity of cortical and cancellous bone in the posterior mandible increase peri-implant stress and strain under oblique loading. *Clinical Oral Implants Research*, 12:648–657, 2001.

[27] A. Mellal, H.W.A. Wiskott, J. Botsis, S.S. Scherrer, and U.C. Belser. Stimulating effect of implant loading on surrounding bone. Comparison of three numerical models and validation by *in vivo* data. *Clinical Oral Implants Research*, 15:239–248, 2004.

[28] H. Van Oosterwyck, J. Duyck, J. Vander Sloten, G. Van der Perre, M. De Cooman, S. Lievens, R. Puers, and I. Naert. The influence of bone mechanical properties and implant fixation upon bone loading around oral implants. *Clinical Oral Implants Research*, 9:407–418, 1998.

[29] H. Van Oosterwyck, J. Duyck, J. Vander Sloten, G. Van der Perre, and I. Naert. Peri-implant bone tissue strains in cases of dehiscence: a finite element study. *Clinical Oral Implants Research*, 13:327–333, 2002.

[30] F. Zarone, A. Apicella, L. Nicolais, R. Aversa, and R. Sorrentino. Mandibular flexure and stress build-up in mandibular full-arch fixed prostheses supported by osseointegrated implants. *Clinical Oral Implants Research*, 14:103–114, 2003.

[31] K. Akça, M.C. Çehreli, and H. İplikçioğlu. Evaluation of the mechanical characteristics of the implant-abutment complex of a reduced-diameter morse-taper implant. *Clinical Oral Implants Research*, 14:444–454, 2003.

[32] H.-J. Chun, S.-Y. Cheong, J.-H. Han, S.-J. Heo, J.-P. Chung, I.-C. Rhyu, Y.-C. Choi, H.-K. Baik, Y. Ku, and M.-H. Kim. Evaluation of design parameters of osseointegrated dental implants using finite element analysis. *Journal of Oral Rehabilitation*, 29:565–574, 2002.

[33] J.P. Geng, Q.S. Ma, W. Xu, K.B.C. Tan, and G.R. Liu. Finite element analysis of four thread-form configurations in a stepped screw implant. *Journal of Oral Rehabilitation*, 31:233–239, 2004.

[34] S. Hansson. The implant neck: smooth or provided with retention elements. *Clinical Oral Implants Research*, 10:394–405, 1999.

[35] S. Hansson. A conical implant-abutment interface at the level of the marginal bone improves the distribution of stress in the support bone. *Clinical Oral Implants Research*, 14:286–293, 2002.

[36] L. Lang, B. Kang, R.-F. Wang, and B. Lang. Finite element analysis to determine implant preload. *The Journal of Prosthetic Dentistry*, 90(6):539–546, 2003.

[37] H.-M. Huang, S.-Y. Lee, and C.-Y. Yeh C.-T. Lin. Resonance frequency assessment of dental implant stability with various bone qualities: a numerical approach. *Clinical Oral Implants Research*, 13:65–74, 2002.

[38] K.R. Williams and A.D.C. Williams. Impulse response of a dental implant in bone by numerical analysis. *Biomaterials*, 18:715–719, 1997.

[39] Stephen Cowin. *Bone Mechanics Handbook*. CRC Press, 2001.

[40] Robert Blevins. *Formulas for Natural Frequency and Mode Shape.* Robert E. Krieger Publishing Company, 1979.

[41] Stephen Hurst. Investigation of Periotest® and Osstell® instruments for measuring craniofacial implant integrity. Master's thesis, University of Alberta, 2002.

[42] William T. Thomson. *Theory of Vibration with Applications - 5th Edition.* Prentice-Hall, Inc., 1998.

[43] K.-J. Bathe. *Finite Element Procedures in Engineering Analysis.* Prentice-Hall, 1982.

[44] E.L. Wilson and T. Itoh. An eigensolution strategy for large systems. *Computers and Structures*, 16(1-4):259–265, 1983.

[45] ANSYS Inc, Canonsburb, Pa. *ANSYS 7.1 Documentation - Element Reference - Part I. Element Library - SOLID45.*

[46] ANSYS Inc, Canonsburb, Pa. *ANSYS 7.1 Documentation - Element Reference - Part I. Element Library - SOLID92.*

[47] Polymer material properties, 2004.

[48] ANSYS Inc, Canonsburb, Pa. *ANSYS 7.1 Documentation - Element Reference - Part I. Element Library - CONTA174.*

[49] ANSYS Inc, Canonsburb, Pa. *ANSYS 7.1 Documentation - Element Reference - Part I. Element Library - TARGE170.*

[50] ANSYS Inc, Canonsburb, Pa. *ANSYS 7.1 Documentation - Structural Guide - Chapter 11: Contact.*

[51] Erwin Kreyszig. *Advanced Engineering Mathematics.* John Wiley and Sons Inc, seventh edition, 1993.

[52] T. Chandrupatla and A. Belegundu. *Introduction to Finite Elements in Engineering.* Prentice Hall Inc, third edition, 2002.

[53] J. C. Simo and T. A. Laursen. An augmented lagrangian treatment of contact problems involving friction. *Computers and Structures*, 42:97–116, 1992.

[54] Michel Fortin and Ronald Glowinski. *Augmented Lagrangian Methods.* Elsevier Science Pub. Co., 1983.

[55] Ronald Glowinski and Patrick Le Tallec. *Augmented Lagrangian and operator-splitting methods in nonlinear mechanics.* SIAM Studies in Applied Mathematics, Philadelphia, 1989.

[56] B. Brunski. In vivo bone response to biomechanical loading at the bone/dental-implant interface. *Advances in Dental Research*, 13:99–119, 1999.

[57] M.L. James, G.M Smith, J.C. Wolford, and P.W. Whaley. *Vibration of Mechanical and Structural Systems - 2nd Edition.* HarperCollins, 1994.

[58] ANSYS Inc, Canonsburb, Pa. *ANSYS 7.1 Documentation - Structural Guide - Chapter 3: Modal Analysis.*

[59] ANSYS Inc, Canonsburb, Pa. *ANSYS 7.1 Documentation - Theory Reference - Chapter 17: Analysis Procedures.*

[60] Singiresu Rao. *Mechanical Vibrations.* Addison-Wesley Publishing Company, second edition, 1990.

Appendix A

FEA Example

Consider the rod shown in Figure A.1. The analytical solution for the deflection of the end of the rod is:

$$\delta = \frac{PL}{EA} = 1mm \tag{A.1}$$

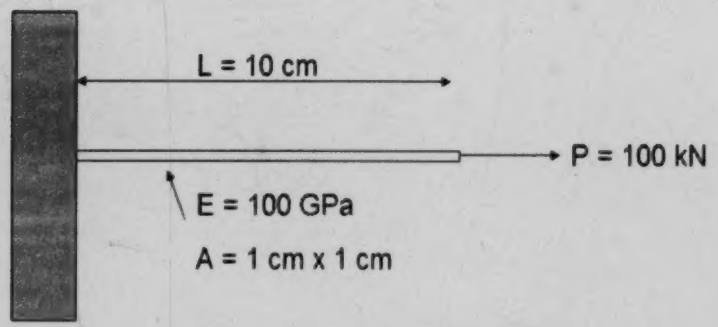

Figure A.1: FEA Example Rod

Imagine the rod is divided into three elements, resulting in the nodes depicted in Figure A.2.

Bathe [43] shows that the governing equation for a linear rod element is:

$$\frac{EA}{\ell}\begin{bmatrix} 1 & -1 \\ -1 & 1 \end{bmatrix}\begin{pmatrix} u_1 \\ u_2 \end{pmatrix} = \begin{pmatrix} F_1 \\ F_2 \end{pmatrix} \tag{A.2}$$

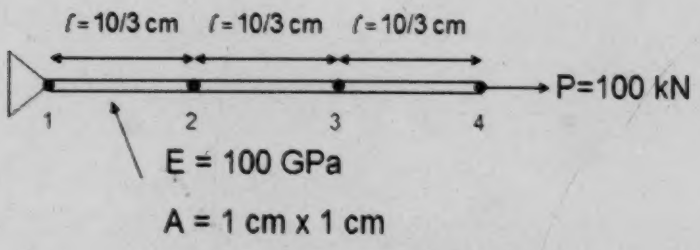

Figure A.2: Finite Element Representation of Rod

where $\ell = \frac{L}{3}$ in this case. Thus, using the global stiffness matrix construction technique outlined in Appendix B, the problem can be written as:

$$\frac{3EA}{L}\begin{bmatrix} 1 & -1 & 0 & 0 \\ -1 & 2 & -1 & 0 \\ 0 & -1 & 2 & -1 \\ 0 & 0 & -1 & 1 \end{bmatrix}\begin{pmatrix} u_1 \\ u_2 \\ u_3 \\ u_4 \end{pmatrix} = \begin{pmatrix} F_1 \\ F_2 \\ F_3 \\ F_4 \end{pmatrix} \tag{A.3}$$

The boundary conditions state that displacement at $u_1 = 0$ and $F_4 = P$. Using the elimination approach, Equation (A.3) can be written as:

$$\frac{3EA}{L}\begin{bmatrix} 2 & -1 & 0 \\ -1 & 2 & -1 \\ 0 & -1 & 1 \end{bmatrix}\begin{pmatrix} u_2 \\ u_3 \\ u_4 \end{pmatrix} = \begin{pmatrix} 0 \\ 0 \\ P \end{pmatrix} \tag{A.4}$$

The displacement vector can be solved using $\{u\} = [k]^{-1}\{F\}$ thus:

$$\begin{pmatrix} u_2 \\ u_3 \\ u_4 \end{pmatrix} = \frac{L}{3EA}\begin{bmatrix} 1 & 1 & 1 \\ 1 & 2 & 2 \\ 1 & 2 & 3 \end{bmatrix}\begin{pmatrix} 0 \\ 0 \\ P \end{pmatrix} \tag{A.5}$$

gives:

$$\{u\} = \frac{PL}{3EA}\begin{pmatrix} 1 \\ 2 \\ 3 \end{pmatrix} \tag{A.6}$$

Therefore, the displacement of the end of the rod is $u_3 = \frac{PL}{EA} = 1mm$ which matches the analytical result.

Appendix B

Modal Participation Factors from a Continuous System Approximation

If it can be shown that the natural frequencies of a finite DOF system approximating a simple continuous system converge to the continuous solution then it is reasonable to approximate a continuous system too complex to solve analytically in the same manner. A finite approximation of a rigidly fixed, uniform cantilever will be solved to prove feasibility and then the procedure will be used to approximate the modal participation factors of the first three natural frequencies of an elastically supported beam with a mass on the free end. This complex system is similar to the implant - abutment system being struck by the impact rod and the solution will be used to determine the plausibility of only two natural frequencies being visible on the accelerometer signal.

B.1 Governing Equation

Thomson [42] shows that if synchronous motion is assumed, the governing equation for the system:

$$[m]\{\ddot{u}\} + [k]\{u\} = \{0\} \tag{B.1}$$

can be used to determine the natural frequencies and corresponding mode shapes by solving the eigenvalue problem:

$$|[k] - p^2[m]| = 0 \tag{B.2}$$

Therefore it is necessary to determine the stiffness matrix $[k]$ and the mass matrix $[m]$.

B.2 Constructing the Stiffness Matrix

The governing equation for a single beam element with two degrees of freedom at each node (vertical displacement and rotation) is the following:

$$\frac{EI}{L^3}\begin{bmatrix} 12 & 6L & -12 & 6L \\ 6L & 4L^2 & -6L & 2L^2 \\ -12 & -6L & 12 & -6L \\ 6L & 2L^2 & -6L & 4L^2 \end{bmatrix}\begin{pmatrix} v_1 \\ \theta_1 \\ v_2 \\ \theta_2 \end{pmatrix} = \begin{pmatrix} F_1 \\ T_1 \\ F_2 \\ T_2 \end{pmatrix} \tag{B.3}$$

Recall that a global stiffness matrix can be assembled from elementary stiffness matrices. For example, if there are two beam elements with stiffness matrix $[k]$ and $[K]$ respectively, connected at node 2, they can be assembled as follows:

$$\begin{bmatrix} k_{11} & k_{12} & k_{13} & k_{14} & 0 & 0 \\ k_{21} & k_{22} & k_{23} & k_{24} & 0 & 0 \\ k_{31} & k_{32} & k_{33}+K_{11} & k_{34}+K_{12} & K_{13} & K_{14} \\ k_{41} & k_{42} & k_{43}+K_{21} & k_{44}+K_{22} & K_{23} & K_{24} \\ 0 & 0 & K_{31} & K_{32} & K_{33} & K_{34} \\ 0 & 0 & K_{41} & K_{42} & K_{43} & K_{44} \end{bmatrix}\begin{pmatrix} v_1 \\ \theta_1 \\ v_2 \\ \theta_2 \\ v_3 \\ \theta_3 \end{pmatrix} = \begin{pmatrix} F_1 \\ T_1 \\ F_2 \\ T_2 \\ F_3 \\ T_3 \end{pmatrix} \tag{B.4}$$

If a linear spring were connected from node 1 to the ground, depicted in

Figure B.1, the governing equation would become:

$$\begin{bmatrix} k_{11}+k_s & k_{12} & k_{13} & k_{14} & 0 & 0 & k_s & 0 \\ k_{21} & k_{22} & k_{23} & k_{24} & 0 & 0 & 0 & 0 \\ k_{31} & k_{32} & k_{33}+K_{11} & k_{34}+K_{12} & K_{13} & K_{14} & 0 & 0 \\ k_{41} & k_{42} & k_{43}+K_{21} & k_{44}+K_{22} & K_{23} & K_{24} & 0 & 0 \\ 0 & 0 & K_{31} & K_{32} & K_{33} & K_{34} & 0 & 0 \\ 0 & 0 & K_{41} & K_{42} & K_{43} & K_{44} & 0 & 0 \\ k_s & 0 & 0 & 0 & 0 & 0 & k_s & 0 \\ 0 & 0 & 0 & 0 & 0 & 0 & 0 & 0 \end{bmatrix} \begin{pmatrix} v_1 \\ \theta_1 \\ v_2 \\ \theta_2 \\ v_3 \\ \theta_3 \\ v_g \\ \theta_g \end{pmatrix} = \begin{pmatrix} F_1 \\ T_1 \\ F_2 \\ T_2 \\ F_3 \\ T_3 \\ F_g \\ T_g \end{pmatrix} \tag{B.5}$$

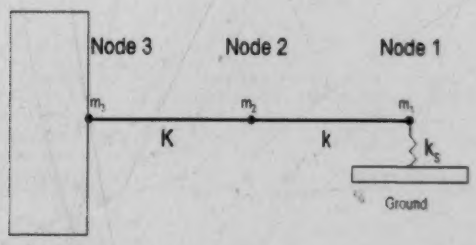

Figure B.1: Cantilever with Spring Attached to Ground

However, since the vertical and rotation displacement of the ground is zero, the corresponding rows and columns of the global stiffness matrix can be eliminated using the elimination approach resulting in the equation below.

$$\begin{bmatrix} k_{11}+k_s & k_{12} & k_{13} & k_{14} & 0 & 0 \\ k_{21} & k_{22} & k_{23} & k_{24} & 0 & 0 \\ k_{31} & k_{32} & k_{33}+K_{11} & k_{34}+K_{12} & K_{13} & K_{14} \\ k_{41} & k_{42} & k_{43}+K_{21} & k_{44}+K_{22} & K_{23} & K_{24} \\ 0 & 0 & K_{31} & K_{32} & K_{33} & K_{34} \\ 0 & 0 & K_{41} & K_{42} & K_{43} & K_{44} \end{bmatrix} \begin{pmatrix} v_1 \\ \theta_1 \\ v_2 \\ \theta_2 \\ v_3 \\ \theta_3 \end{pmatrix} = \begin{pmatrix} F_1 \\ T_1 \\ F_2 \\ T_2 \\ F_3 \\ T_3 \end{pmatrix} \tag{B.6}$$

B.3 Constructing the Mass Matrix

The mass matrix could be constructed in a similar manner, but in order to simplify the calculations a lumped mass approximation was used. A lumped mass approximation is where the mass of the element is applied as two equal masses at the ends of the element. In this case, the lumped mass approximation eliminates any rotational inertia terms in the mass matrix, resulting in

$$\begin{bmatrix} m_1 & 0 & 0 & 0 & 0 & 0 \\ 0 & 0 & 0 & 0 & 0 & 0 \\ 0 & 0 & m_2 & 0 & 0 & 0 \\ 0 & 0 & 0 & 0 & 0 & 0 \\ 0 & 0 & 0 & 0 & m_3 & 0 \\ 0 & 0 & 0 & 0 & 0 & 0 \end{bmatrix} \tag{B.7}$$

This is a reasonable approximation in this case since the elements are undergoing small deflections thus little rotation is occurring. In the case of a point mass, the extra mass, M, can be added to the appropriate node.

Since the rotational terms in the mass matrix are zero, it is beneficial to rearrange the stiffness matrix to simplify calculations.

B.4 Matrix Partitioning for Coordinate Reduction

By rearranging the global mass and stiffness matrix so that the coordinates arranged as

$$\begin{pmatrix} v_1 \\ v_2 \\ v_3 \\ \theta_1 \\ \theta_2 \\ \theta_3 \end{pmatrix} = \begin{pmatrix} V \\ \theta \end{pmatrix} \tag{B.8}$$

results in the following equation

$$\begin{bmatrix} M_{11} & 0 \\ 0 & 0 \end{bmatrix} \begin{pmatrix} \ddot{V} \\ \ddot{\theta} \end{pmatrix} + \begin{bmatrix} J_{11} & J_{12} \\ J_{21} & J_{22} \end{bmatrix} \begin{pmatrix} V \\ \theta \end{pmatrix} = \begin{pmatrix} 0 \\ 0 \end{pmatrix} \tag{B.9}$$

As shown in [42], this can be manipulated to:

$$M_{11}\ddot{V} + HV = 0 \tag{B.10}$$

where

$$H = (J_{11} - J_{12}J_{22}^{-1}J_{21}) \tag{B.11}$$

Equation (B.10) is an eigenvalue problem if it is assumed $\ddot{V} = -p^2V$ and can be solved for the natural frequencies and vertical displacement mode shapes of the system as explained in [42].

B.5 Comparison to Continuous Cantilever

Using the methods outlined above, the system depicted in Figure B.2 was constructed in MATLAB using the code found in Appendix F, Section F.1. To simulate the rigidly constrained cantilever, the spring stiffness, k_s, was increased until the first natural frequency for a 50 element system converged below 1%, effectively turning the springs into rigid bodies. In this case, what is called the effective length of the system in the MATLAB code is half the total length of the cantilever since only half of the total beam is free to move. The point mass was not included. With these parameters, the first three natural frequencies converged below 1% with 200 elements.

The continuous system has natural frequencies given by:

$$p_n = (\beta L)_n^2\sqrt{\frac{EI}{\rho AL^4}} \tag{B.12}$$

In order to simplify comparisons, the (βL) term of the first three frequencies from the finite system are listed below.

System	$(\beta L)_1$	$(\beta L)_2$	$(\beta L)_3$
Continuous	1.875	4.694	7.855
Finite	1.870	4.680	7.832

Table B.1: (βL) Comparisons of Continuous and Finite Systems

The finite system converged within 0.3% relative error for the first three theoretical (βL) values. Therefore, simulating a continuous system with a finite DOF model is acceptable.

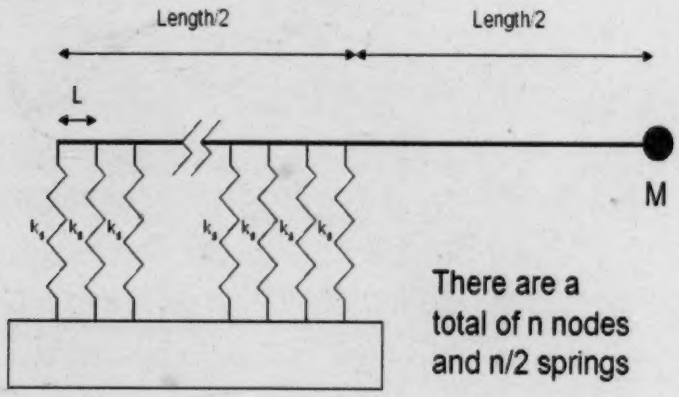

Figure B.2: Model Approximating Elastically Supported Beam with Point Mass

The case of an elastically supported beam with a point mass on the free end (Fig B.2) is used as a more accurate representation of the implant - abutment system. The point mass was assumed to be 13 times the mass of the total beam, which is analogous to the implant system (9 gram impact rod, 0.7 gram aluminum post). However, this model is merely an approximation. It does not take into account displacements along the axis of the beam and the stiffnesses of the supporting springs are not accurate. It does however provide a reasonable platform to determine the plausibility of only two natural frequencies being visible on the accelerometer signal.

The stiffnesses of the springs were reduced until the first three expected mode shapes were found, depicted in Figure B.3. The first two of these mode shapes are predicted by Hurst [41] and the third is assumed to be a bending mode. The number of elements was increased until the first three natural frequencies converged below 1% (200 elements). At this point the model was assumed to be a realistic representation of the continuous system. The (βL) were not recorded as they are not of interest in this case. Instead, the modal participation factors of the first three natural frequencies are desired.

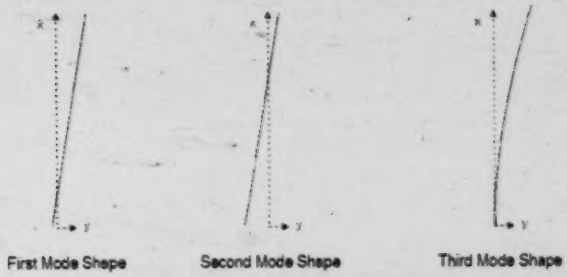

Figure B.3: First Three Expected Mode Shapes

B.6 Determining Modal Participation Factors

The mode shapes can be normalized to the mass matrix and combined to form the modal matrix, as detailed in [57]. If synchronous motion is assumed, the displacement vector can be written as:

$$\{x(t)\} = [u]\{\eta(t)\} \tag{B.13}$$

so:

$$\{\ddot{x}(t)\} = [u]\{\ddot{\eta}(t)\} \tag{B.14}$$

Using this substitution the governing equation can be transformed to:

$$\{\ddot{\eta}\} + \begin{bmatrix} \ddots & & \\ & p^2 & \\ & & \ddots \end{bmatrix} \{\eta\} = \{0\} \tag{B.15}$$

Therefore

$$\ddot{\eta}_r + p_r^2 \eta_r = 0 \tag{B.16}$$

These n equations can be solved for the n η's individually since the equations have been uncoupled. However, it is first necessary to determine the initial conditions of the system. This system is approximating the implant - abutment during a strike from the impact rod, thus the IC's of that system will be used. Since it is difficult to accurately determine the shape of the forcing function caused during the duration of the strike, the transient

response of the system was not used. Instead, the strike can be considered an impulse over a short period of time thus there is an initial velocity vector while the initial displacement vector remain zero. To determine the initial velocity vector it was assumed the implant would rotate about its lowest node, O (similar to the first mode shape) and angular momentum would be conserved as depicted in Figure B.4.

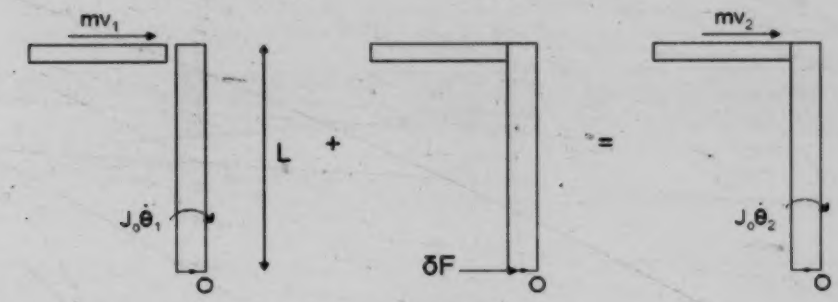

Figure B.4: Momentum Diagram

Conserving angular momentum about the base of the implant and realizing $\dot{\theta}_1 = 0$:

$$mv_1 L = mv_2 L + J\dot{\theta}_2 \tag{B.17}$$

$\dot{\theta}_2 = \frac{v_2}{L}$ and $J = \frac{1}{3}ML^2$ so:

$$mv_1 = mv_2 + \frac{1}{3}Mv_2 \tag{B.18}$$

thus v_2 is:

$$v_2 = \frac{mv_1}{m + \frac{1}{3}M} \tag{B.19}$$

Since the implant is rotating about its base, the angular velocity is $\omega = \frac{v_2}{L}$. Therefore, the initial velocity of any point on the implant is given by ωr, where r is the distance measured from the bottom of the implant. Using this relationship and knowing the impact rod strikes the implant at $0.2m/s$, it was possible to determine the initial velocity vector for the implant.

Using the general solution for Equation (B.16) with only an initial velocity results in:

$$\eta_r(t) = \frac{\dot{\eta}_r(0)}{p_r}\sin(p_r t) \tag{B.20}$$

and using Equation (B.13) means that the equation of motion of the end of the beam (node n), where the impact is taking place and thus the signal is being recorded, is equal to:

$$x_n(t) = [u](n,:) \cdot \{\eta(t)\} \tag{B.21}$$

The modal participation factors (MPF) are found as:

$$x_n(t) = MPF_1 \sin(p_1 t) + MPF_2 \sin(p_2 t) + MPF_3 \sin(p_3 t) + ... \tag{B.22}$$

The values in Table B.2 were found using the MATLAB code. The first natural frequency has a MPF approximately 24 times greater than the second and 1400 times greater than the third. This would suggest that it is plausible that only the first two frequencies would be visible from the accelerometer signal when struck at the top of the implant.

Natural Frequency	MPF
$1st$	$3.02\text{x}10^{-2}$
$2nd$	$-1.26\text{x}10^{-3}$
$3rd$	$2.21\text{x}10^{-5}$

Table B.2: Modal Participation Factors for First Three Natural Frequencies

Note: If instead of assuming the aluminium post rotates about its lowest node but rather is free, this results in:

$$v_2 = \frac{mv_1}{m + \frac{1}{4}M} \tag{B.23}$$

$$\omega = \frac{3v_2}{2L} \tag{B.24}$$

The first natural frequency then has a MPF approximately 24 times greater than the second and 1360 times greater than the third. Therefore the MPF's are similar in both of these cases. Note that the actual physical system would be expected to fall somewhere between these two systems.

Appendix C

Subspace Modal Solver

At first glace, the subspace method seems to be a very simple process. In application this is true, which is the beauty of the method. However, the mathematical theory behind the method is anything but simple. For further details and proofs, refer to Bathe [43] and the ANSYS reference manual [58]. This appendix is merely an overview of the process.

The subspace iteration method solves for p eigenvalues and corresponding eigenvectors which satisfy:

$$[K][\mu] = [M][\mu][\lambda] \tag{C.1}$$

where $[\mu] = [\mu_1, \mu_2, ..., \mu_p]$ and $[\lambda] = diag(\lambda_i)$. These eigenvectors also must satisfy the orthogonality conditions:

$$[\mu]^T[K][\mu] = [\lambda] \tag{C.2}$$

$$[\mu]^T[M][\mu] = [I] \tag{C.3}$$

This is accomplished using simultaneous vector inverse iteration:

$$[K][\bar{X}]_{k+1} = [M][X]_k \tag{C.4}$$

$[X]_k$ is the current estimate of the q-dimension subspace spanning a portion of the solution space of Equation (C.1). Since the eigenvectors in Equation (C.1) form an [M]-orthonormal basis of the q-dimensional least-dominant subspace of the operators [K] and [M], the estimate $[X]_k$ will converge towards $[\mu]$.

Choosing the initial estimate $[X]_0$ is an important step and is accomplished automatically in ANSYS as described below. The number of starting

iteration vectors are determined from:

$$q = p + d \tag{C.5}$$

where:
p = the requested number of modes to extract
d = number of extra iteration vectors (defaults to 4)
The d extra vectors are used to increase the convergence rate of the requested modes.

The vectors comprising $[X]_0$ depend if rigid body modes are present. For every rigid-body mode, the position in the vector corresponding to the degree of freedom of which the mode takes place is set to a unit value. The remaining vectors in $[X]_0$ are initialized to random vectors. By randomizing the vectors, ANSYS ensures that all mass DOF's are excited.

With the initial estimate, Equation (C.4) is solved:

$$[\bar{X}]_{k+1} = [K]^{-1}[M][X]_k \tag{C.6}$$

The projections of the operators [K] and [M] onto the q-dimensional subspace are found:

$$[K]_{k+1} = [\bar{X}]_{k+1}^T[K][\bar{X}]_{k+1} \tag{C.7}$$

$$[M]_{k+1} = [\bar{X}]_{k+1}^T[M][\bar{X}]_{k+1} \tag{C.8}$$

The eigenvalue problem for the subspace is solved:

$$[K]_{k+1}[Q]_{k+1} = [M]_{k+1}[Q]_{k+1}[\lambda]_{k+1} \tag{C.9}$$

ANSYS utilizes a generalized Jacobi iteration technique to accomplish this to minimize processing time [43].

Before continuing, the vectors comprising [Q] must be made orthogonal to one another. This is so [Q] satisfies the conditions in Equation (C.3). This is done using the Gram-Schmidt method, described in Section C.1.

From this, an improved approximation of the eigenvectors can be found:

$$[X]_{k+1} = [\bar{X}]_{k+1}[Q]_{k+1} \tag{C.10}$$

This iteration is continued until it has converged and produces the results:

$$[\lambda]_{k+1} \rightarrow [\lambda] \quad and \quad [X]_{k+1} \rightarrow [\mu] \quad as \quad k \rightarrow \infty \tag{C.11}$$

To ensure the values are the desired frequencies, a Strum sequence check is performed. This check computes the number of negative pivots encountered during the formation of $[K]_{k+1}$ [43]. This number should match the number of converged eigenvalues or else an eigenvalue was missed. In this case, more iteration vectors (d) must be used.

Again, the beauty of the subspace method is that the first p natural frequencies and corresponding mode spaces can be found by solving only a q dimensional eigenvalue problem, unlike the general analytical modal method which requires all the natural frequencies to be found.

C.1 Gram-Schmidt Orthogonalization

The purpose of the Gram-Schmidt Orthogonalization technique is to orthogonalize each vector in a matrix to the previous vectors, creating a basis for the space. In this case, the vectors will be [M]-orthogonalized so that Equation (C.3) is satisfied. The process is best described in an example.

Consider the set of vectors and mass matrix:

$$[X] = \begin{bmatrix} 0.25 & 0.75 \\ 0.5 & 0.5 \\ 0.75 & 0.25 \end{bmatrix} \quad [m] = \begin{bmatrix} \frac{1}{2} & 0 & 0 \\ 0 & 1 & 0 \\ 0 & 0 & \frac{1}{2} \end{bmatrix} \tag{C.12}$$

To create a basis for the plane which satisfies Equation (C.3), first [m]-normalize the first vector:

$$\alpha_1^2 \begin{pmatrix} 0.25 & 0.5 & 0.75 \end{pmatrix} \begin{bmatrix} \frac{1}{2} & 0 & 0 \\ 0 & 1 & 0 \\ 0 & 0 & \frac{1}{2} \end{bmatrix} \begin{pmatrix} 0.25 \\ 0.5 \\ 0.75 \end{pmatrix} = 1 \tag{C.13}$$

thus:

$$\alpha_1 = \frac{4}{3} \tag{C.14}$$

so the [m]-normalized vector is:

$$\alpha_1 \begin{pmatrix} 0.25 \\ 0.5 \\ 0.75 \end{pmatrix} = \begin{pmatrix} 1/3 \\ 2/3 \\ 1 \end{pmatrix} \tag{C.15}$$

therefore:

$$[X]^* = \begin{bmatrix} 1/3 & 0.75 \\ 2/3 & 0.5 \\ 1 & 0.25 \end{bmatrix} \tag{C.16}$$

At this point the Gram-Schmidt method is employed using the following equation:

$$\{u\}_j = \{v\}_j - \sum_{i=1}^{j-1} \beta_i \{\phi\}_i \tag{C.17}$$

where:

$$\beta_i = \{\phi\}_i^T [m] \{v\}_j \tag{C.18}$$

and:
$\{v\}_j$ = the vector to be orthogonalized
$\{u\}_j$ = the new orthogonalized vector
$\{\phi\}_i$ = the vector(s) to which $\{u\}_j$ is orthogonal

In this example:

$$\beta_1 = \begin{pmatrix} 1/3 & 2/3 & 1 \end{pmatrix} \begin{bmatrix} \frac{1}{2} & 0 & 0 \\ 0 & 1 & 0 \\ 0 & 0 & \frac{1}{2} \end{bmatrix} \begin{pmatrix} 0.75 \\ 0.5 \\ 0.25 \end{pmatrix} \Rightarrow \beta_1 = 0.5833 \tag{C.19}$$

Therefore:

$$\{u\}_2 = \{v\}_2 - \beta_1 \{\phi\}_1 \tag{C.20}$$

$$= \begin{pmatrix} 0.75 \\ 0.5 \\ 0.25 \end{pmatrix} - 0.5833 \begin{pmatrix} 1/3 \\ 2/3 \\ 1 \end{pmatrix} \tag{C.21}$$

$$= \begin{pmatrix} 0.5556 \\ 0.1111 \\ -0.3333 \end{pmatrix} \tag{C.22}$$

[m]-normalizing $\{u\}_2$ gives:

$$[X]_2 = \begin{bmatrix} 1/3 & 1.179 \\ 2/3 & 0.2357 \\ 1 & -0.7071 \end{bmatrix} \tag{C.23}$$

which satisfies Equation (C.3).

Appendix D

Transient Solver

The governing equation for motion of a structure is as follows:

$$M\ddot{U} + C\dot{U} + KU = R \tag{D.1}$$

where M, C, and K are the mass, damping, and stiffness matrices; R is the external load vector; and U, $\dot{U}$, and $\ddot{U}$ are the displacement, velocity and acceleration vectors of the finite element analysis. This equation represents a system of second-order, linear differential equations and can be solved by any number of standard procedures. However, for general systems with large matrices, these standard procedures can be very computationally expensive. The procedure used for Transient Analyses by ANSYS is the Newmark Method.

The Newmark method falls into the category of direct integration methods. "In direct integration the equations in (D.1) are integrated using a numerical step-by-step procedure, the term "direct" meaning that prior to the numerical integration, no transformation of the equations into a different form is carried out." [43] The theory is largely based on two ideas. First, rather than satisfying equation (D.1) for any time, t, it is only necessary to satisfy (D.1) at discrete time intervals Δt apart. Thus the problem can be considered quasi-static, which includes the effect of inertia and damping forces, and solved as such. The second idea is that it is assumed the displacement, velocity and accelerations within each time interval, Δt, vary slightly. It is the form of these assumptions that determines the accuracy, stability and cost of the solution procedure. For a direct integration method it is necessary to know the initial conditions so that displacement, velocity and

acceleration are known at time $t = 0$ and can be used to find subsequent values during the next time interval.

The Newmark method proposes that [43]:

$$\{\dot{u}_{n+1}\} = \{\dot{u}_n\} + [(1-\delta)\{\ddot{u}_n\} + \delta\{\ddot{u}_{n+1}\}]\Delta t \tag{D.2}$$

$$\{u_{n+1}\} = \{u_n\} + \{\dot{u}_n\}\Delta t + \left[\left(\frac{1}{2} - \alpha\right)\{\ddot{u}_n\} + \alpha\{\ddot{u}_{n+1}\}\right]\Delta t^2 \tag{D.3}$$

where:
α, δ = Newmark integration parameters
$\Delta t = t_{n+1} - t_n$
$\{u_n\}$ = nodal displacement vector at time t_n
$\{\dot{u}_n\}$ = nodal velocity vector at time t_n
$\{\ddot{u}_n\}$ = nodal acceleration vector at time t_n
$\{u_{n+1}\}$ = nodal displacement vector at time t_{n+1}
$\{\dot{u}_{n+1}\}$ = nodal velocity vector at time t_{n+1}
$\{\ddot{u}_{n+}\}$ = nodal acceleration vector at time t_{n+1}

The aim is to solve Equation (D.1) for $n + 1$ thus it is helpful to rewrite Equations (D.2) and (D.3) as follows (see below for α_n values in terms of α, δ and Δt):

$$\{\ddot{u}_{n+1}\} = a_0(\{u_{n+1}\} - \{u_n\}) - a_2\{\dot{u}_n\} - a_3\{\ddot{u}_n\} \tag{D.4}$$

$$\{\dot{u}_{n+1}\} = \{\dot{u}_n\} + a_6\{\ddot{u}_n\} + a_7\{\ddot{u}_{n+1}\} \tag{D.5}$$

Noting that Equation (D.4) can be subbed into Equation (D.5) to give:

$$\{\dot{u}_{n+1}\} = \{u_{n+1}\}[a_0a_7] - \{u_n\}[a_0a_7] - \{\dot{u}_n\}[a_2a_7 - 1] - \{\ddot{u}_n\}[a_3a_7 - a_6] \tag{D.6}$$

and letting:
$a_1 = a_0a_7$
$a_4 = a_2a_7 - 1$
$a_5 = a_3a_7 - a_6$
This finally gives:

$$\{\ddot{u}_{n+1}\} = a_0\{u_{n+1}\} - a_0\{u_n\} - a_2\{\dot{u}_n\} - a_3\{\ddot{u}_n\} \tag{D.7}$$

$$\{\dot{u}_{n+1}\} = a_1\{u_{n+1}\} - a_1\{u_n\} - a_4\{\dot{u}_n\} - a_5\{\ddot{u}_n\} \tag{D.8}$$

where:

$$a_0 = \frac{1}{\alpha \Delta t^2} \qquad a_1 = \frac{\delta}{\alpha \Delta t}$$
$$a_2 = \frac{1}{\alpha \Delta t} \qquad a_3 = \frac{1}{2\alpha} - 1$$
$$a_4 = \frac{\delta}{\alpha} - 1 \qquad a_5 = \frac{\Delta t}{2}\left(\frac{\delta}{\alpha} - 2\right)$$
$$a_6 = \Delta t(1 - \delta) \qquad a_7 = \delta \Delta t$$

Notice how Equations (D.7) and (D.8) are only functions of $\{u_{n+1}\}$ and other known values.

Substituting these values into Equation (D.1) at $n + 1$ gives:

$$(a_0[M] + a_1[C] + [K])\{u_{n+1}\} = \{R\} + [M](a_0\{u_n\} + a_2\{\dot{u}_n\} + a_3\{\ddot{u}_n\}) + [C](a_1\{u_n\} + a_4\{\dot{u}_n\} + a_5\{\ddot{u}_n\}) \quad \text{(D.9)}$$

Equation (D.9) is used to solve for $\{u_{n+1}\}$ as it is the only unknown.

Newmark showed that if:

$$\alpha = \frac{1}{4}(1 + \gamma)^2 \qquad \delta = \frac{1}{2} + \gamma \qquad \text{(D.10)}$$

the solution is unconditionally stable for $\gamma \geq 0$. By default γ is set to 0.005 in ANSYS in order to optimize numerical damping during the transient analysis. Numerical damping is used to improve the accuracy of higher natural frequencies by reducing the amount of numerical noise introduced during the solution calculations.

The HHT improvement algorithm is used in conjunction with the Newmark method in ANSYS. It has an improved level of numerical damping in order to reduce calculation times and improve convergence. It introduces two other variables but follows the same procedure as the basic Newmark method. For further information see [59].

Appendix E

Analytical Second Natural Frequency

The following outlines the procedure used to solve for the first two (βL) values for an analytical solution to the lateral vibrations problem of a cantilever with a concentrated mass at the free end. This solution will be used to calculate the first and second natural frequency of the system which will be compared to the solution of a transient FEA simulation of a similar beam to determine if the FEA simulation produces reasonable second mode results.

Consider the bending vibrations of the bar below.

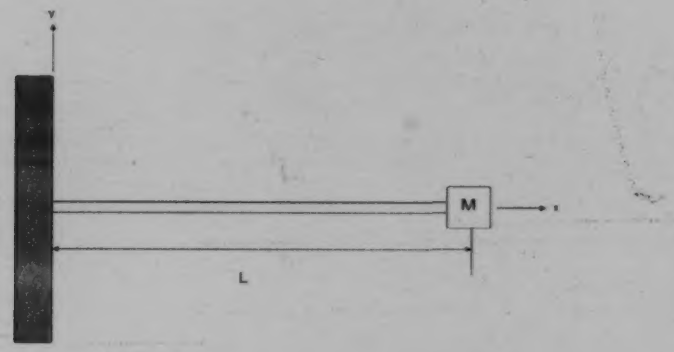

Figure E.1: Analytical Model to Verify Second Mode of Vibration

$$y(x,t) = Y(x)T(t)$$

where

$$Y(x) = C_1\sin(\beta x) + C_2\cos(\beta x) + C_3\sinh(\beta x) + C_4\cosh(\beta x)$$

and

$$T(t) = A\sin(pt + \phi)$$

E.1 Boundary Conditions

$x = 0:$	$y = 0$	No displacement	$\Rightarrow Y(0) = 0$	(E.1)
	$\dfrac{\partial y}{\partial x} = 0$	Zero Slope	$\Rightarrow \left.\dfrac{dY}{dx}\right\|_{x=0} = 0$	(E.2)
$x = L:$	$\dfrac{\partial^2 y}{\partial x^2} = 0$	No moment	$\Rightarrow \left.\dfrac{d^2Y}{dx^2}\right\|_{x=L} = 0$	(E.3)

and

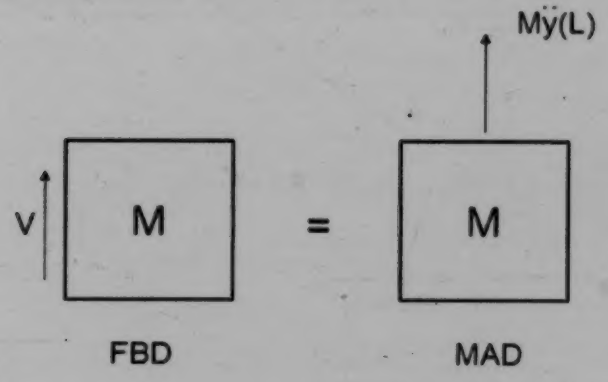

Figure E.2: FBD/MAD of Point Mass

$$V = M\ddot{y}(L)$$

where [60]

$$V = EI\frac{\partial^3 y}{\partial x^3}$$
$$\ddot{y} = \frac{\partial^2 y}{\partial t^2}$$

therefore

$$EI\frac{\partial^3 y}{\partial x^3}\Big|_{x=L} = M\frac{\partial^2 y}{\partial t^2}\Big|_{x=L} \tag{E.4}$$

E.2 Solve for (βL)

$$Y(x) = C_1\sin(\beta x) + C_2\cos(\beta x) + C_3\sinh(\beta x) + C_4\cosh(\beta x) \tag{E.5}$$

From (E.1)

$$Y(0) = 0 = C_1\sin(0) + C_2\cos(0) + C_3\sinh(0) + C_4\cosh(0)$$
$$Y(0) = 0 = C_2 + C_4$$

$$C_4 = -C_2 \tag{E.6}$$

From (E.2)

$$\frac{dY}{dx}\Big|_{x=0} = 0 = C_1\beta\cos(0) - C_2\beta\sin(0) + C_3\beta\cosh(0) + C_4\beta\sinh(0)$$
$$\frac{dY}{dx}\Big|_{x=0} = 0 = C_1 + C_3$$

$$C_3 = -C_1 \tag{E.7}$$

Substitute (E.6) and (E.7) into (E.5)

$$Y(x) = C_1[\sin(\beta x) - \sinh(\beta x)] + C_2[\cos(\beta x) - \cosh(\beta x)]$$
$$\frac{dY}{dx} = C_1\beta[\cos(\beta x) - \cosh(\beta x)] + C_2\beta[-\sin(\beta x) - \sinh(\beta x)]$$
$$\frac{d^2Y}{dx^2} = C_1\beta^2[-\sin(\beta x) - \sinh(\beta x)] + C_2\beta^2[-\cos(\beta x) - \cosh(\beta x)]$$
$$\frac{d^3Y}{dx^3} = C_1\beta^3[-\cos(\beta x) - \cosh(\beta x)] + C_2\beta^3[\sin(\beta x) - \sin(\beta x)]$$

From (E.3)

$$C_1\beta^2[-\sin(\beta L)-\sinh(\beta L)]+C_2\beta^2[-\cos(\beta L)-\cosh(\beta L)]=0 \qquad \text{(E.8)}$$

$$C_1(h_1)+C_2(h_2)=0$$

From (E.4)

$$EI\frac{\partial^3 y}{\partial x^3}\Big|_{x=L}=M\frac{\partial^2 y}{\partial t^2}\Big|_{x=L}$$

$$y(x,t)=Y(x)T(t)$$

$$\frac{\partial^3 y}{\partial x^3}\Big|_{x=L}=\frac{d^3Y}{dx^3}\Big|_{x=L}T(t) \qquad \frac{\partial^2 y}{\partial t^2}\Big|_{x=L}=Y(L)\frac{d^2T}{dt^2}$$

$$EI\frac{d^3Y}{dx^3}\Big|_{x=L}T(t)=MY(L)\left(-p^2T(t)\right)$$

$$EI\frac{d^3Y}{dx^3}\Big|_{x=L}=-Mp^2Y(L) \qquad \text{(E.9)}$$

Substitute into (E.9)

$$EI\left[C_1\beta^3[-\cos(\beta L)-\cosh(\beta L)]+C_2\beta^3[\sin(\beta L)-\sinh(\beta L)]\right]$$
$$=-Mp^2\left[C_1[\sin(\beta L)-\sinh(\beta L)]+C_2[\cos(\beta L)-\cosh(\beta L)]\right]$$

or

$$C_1\left[EI\beta^3[-\cos(\beta L)-\cosh(\beta L)]+Mp^2[\sin(\beta L)-\sinh(\beta L)]\right.$$
$$\left.+C_2\left[EI\beta^3[\sin(\beta L)-\sinh(\beta L)]+Mp^2[\cos(\beta L)-\cosh(\beta L)]\right]=0\right. \qquad \text{(E.10)}$$

$$C_1(j_1)+C_2(j_2)=0$$

Placing Equations (E.8) and (E.10) in matrix form:

$$\begin{bmatrix} h_1 & h_2 \\ j_1 & j_2 \end{bmatrix}\begin{pmatrix} C_1 \\ C_2 \end{pmatrix}=\begin{pmatrix} 0 \\ 0 \end{pmatrix}$$

For a non-trivial C_1 and C_2 we require the determinant to be zero.

$$[EI\beta^3[\sin(\beta L) - \sinh(\beta L)] + Mp^2[\cos(\beta L) - \cosh(\beta L)]] [-\sin(\beta L) - \sinh(\beta L)]$$
$$+[EI\beta^3[-\cos(\beta L) - \cosh(\beta L)] + Mp^2[\sin(\beta L) - \sinh(\beta L)]] [\cos(\beta L) - \cosh(\beta L)] = 0$$

Simplifying

$$EI\beta^3 [-2 (1 + \cos(\beta L) \cosh(\beta L))]$$
$$+ Mp^2 [2 (\sin(\beta L) \cosh(\beta L) - \cos(\beta L) \sinh(\beta L))] = 0 \quad \text{(E.11)}$$

However, for a beam vibrating laterally

$$p = (\beta L)^2 \sqrt{\left(\frac{EI}{m_b L^3}\right)}$$

Substitute into (E.11):

$$1 + \cos(\beta L) \cosh(\beta L) - \frac{M}{m_b}(\beta L) [\sin(\beta L) \cosh(\beta L) - \cos(\beta L) \sinh(\beta L)] = 0 \quad \text{(E.12)}$$

The first two (βL) values that satisfy this equation using the properties listed in Table 2.1 are 0.5776 and 3.9311.

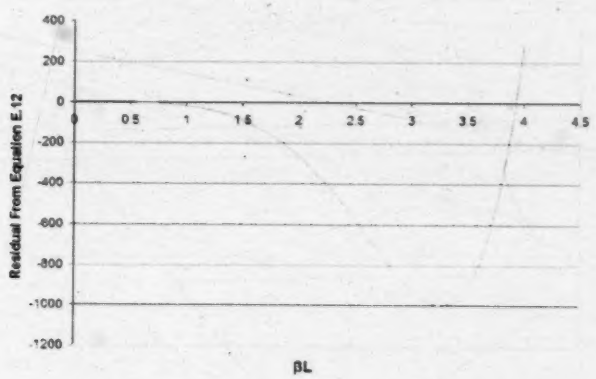

Figure E.3: Plot of Residuals from E.12 Used to find βL Values

Appendix F

ANSYS and MATLAB Code

F.1 MATLAB Code for Analytical Analysis of Modal Participation Factors

```
clear

num = 200;                                  % Number of elements

E = 72e9;                                   % Beam stiffness
I = pi/4*(2e-3)^4;                          % Moment of Inertia
Length = 20e-3;                             % Total length
eff_length = Length;                        % "Effective" Length
L = Length/num;                             % Length of element
A = pi*(2e-3)^2;                            % Area of beam
ro = 2800;                                  % Density of beam

k = 0.00000001 *E*I/L^3;                    % Support spring stiffness

% Initial velocity of rod
v0 = (ro*A*Length)*0.2/(ro*A*Length + 13/3*ro*A*Length);

% Element Stiffness
one_stiff = E*I/L^3 * [12 6*L -12 6*L;6*L 4*L^2 -6*L 2*L^2;
                      ...-12 -6*L 12 -6*L;6*L 2*L^2 -6*L 4*L^2];
```

```
% Initialize global stiffness matrix
stiff = zeros(2*num+2);

% Create global stiffness matrix
for i=1:num
    stiff((2*i-1):(2*i+2),(2*i-1):(2*i+2)) =
          ...stiff((2*i-1):(2*i+2),(2*i-1):(2*i+2)) + one_stiff;
end

half = length(stiff)/2;                    % Half the number of nodes

for y=1:2:half                             % Add a support spring to
    stiff(y,y) = stiff(y,y) + k;           %vertical component of first
end                                        %half of nodes

mass = zeros(half);                        % Initialize mass matrix

mass = eye(half)*ro*A*L;
mass(1,1) = ro*A*L/2;                      % Mass of first node
mass(half,half) = ro*A*L/2 + 13*ro*A*Length;    % Mass of last node

inter_stiff = zeros(2*num + 2);            % Initialize two matrices
                                           %to transform the stiffness

new_stiff = zeros(2*num + 2);              % matrix into lumped mass form

for j = 1:num+1                                % Move all displacement
    inter_stiff(j,:) = stiff((2*j-1),:);       %rows to the top of the
    inter_stiff(j+half,:) = stiff((2*j),:); %matrix and rotation to
end                                            %bottom

for x = 1:num+1                                    % Move all
    new_stiff(:,x) = inter_stiff(:,(2*x-1));       %displacement columns
    new_stiff(:,x+half) = inter_stiff(:,(2*x)); %to the left and
end                                                %rotation to the right

K11 = new_stiff(1:half,1:half);            % Break into the four quadrants
```

```
K12 = new_stiff(1:half,half+1:2*half);

K21 = new_stiff(half+1:2*half,1:half);

K22 = new_stiff(half+1:2*half,half+1:2*half);

% Assemble the lumped stiffness matrix
reduced_stiff = K11 - K12*inv(K22)*K21;

% Calculate eigenvalues/vectors
[e,f] = eig(inv(mass)*reduced_stiff);

% Convert to the (betaL) value
sqrt(f(half,half)*ro*A*(eff_length)^4/E/I)

u = zeros(half);            % Initialize the modal matrix
for n = 1:half
    % Normalize the eigenvectors for u
    alph(n) = sqrt(1/((e(:,n))'*mass*(e(:,n))));
    u(:,n) = alph(n)*e(:,n);
end

% Plot the first three mode shapes
figure(1)
plot(u(:,half))
figure(2)
plot(u(:,half-1))
figure(3)
plot(u(:,half-2))

% Check to make sure the u matrix is "correct"
p_squared = u'*reduced_stiff*u;

% Velocity vector
v = zeros(half,1); for m = 1:half
    v(m) = v0 - (v0/half*m);
end
```

```
% Normalized velocity vector
ada_dot = u'*v;

% Normalized displacement vector
for q = 1:half
    ada(q) = ada_dot(q)/sqrt(p_squared(q,q));
end

% Modal Participation Factors
for r = 1:half
    coef(r) = u(half,r)*ada(r);
end

% Print the MPF's to screen
coef(half)
coef(half-1)
coef(half-2)
```

F.2 ANSYS Code for 3-D Modal Verification Model

```
finish
/clear
/CWD,'D:'
/config,nres,10000

/TITLE, 3-D Modal Analysis Verification
/triad,off
/prep7

! Everything is in meters, kilograms, Newtons, seconds!

beam_length = 10e-2
beam_width = 1e-2
beam_thick = 1e-2

beam_stiff = 100e9              ! Young's Modulus

beam_dens = 1000                ! Beam density

beam_pr = 0.3                   ! Poisson's ratio

blc4,0,0,beam_length,beam_width,beam_thick     ! Create geometry

et,1,solid45                    ! Element type (Solid45)

mp,ex,1,beam_stiff              ! Assign material properties
mp,prxy,1,beam_pr
mp,dens,1,beam_dens

esize,1e-3                      ! Element size vmesh,all,all !
Mesh geometry

finish
/solu
```

```
ANTYPE,2

da,5,all,all                    ! Constrain end of beam
MODOPT,SUBSP,1                  ! Subspace solver with one mode
EQSLV,FRONT
MXPAND,1, , ,0

MODOPT,SUBSP,1,0,0, ,OFF
RIGID,
SUBOPT,8,4,5,0,0,ALL

solve
finish

/post1                  ! List solution
set,list
```

F.3 ANSYS Code for 3-D Transient Verification Model

```
finish
/clear
/CWD,'D:'
/config,nres,10000

/TITLE, 3-D Transient Analysis Verification
/triad,off
/prep7

! Everything is in meters, kilograms, Newtons, seconds!

beam_length = 10e-2
beam_width = 1e-2
beam_thick = 1e-2

beam_stiff = 100e9              ! Young's Modulus

beam_dens = 1000                ! Beam density

beam_pr = 0.3                   ! Poisson's ratio

blc4,0,0,beam_length,beam_width,beam_thick      ! Create geometry

et,1,solid45                    ! Element type (Solid45)

mp,ex,1,beam_stiff              ! Assign material properties
mp,prxy,1,beam_pr
mp,dens,1,beam_dens

esize,1e-3                      ! Element size

vmesh,all,all                   ! Mesh geometry

finish
```

```
/solu

ANTYPE,4
TRNOPT,full
lumpm,0

da,5,all,all                    ! Constrain end of beam

nsubst,100,100,100              ! load stepping options
autots,on
neqit,100
outres,all,all

! Force applied
time,1e-4
timint,on
kbc,1
fk,3,fy,50
fk,7,fy,50
lswrite

nsubst,200,200,200              ! load stepping options
autots,on
neqit,100
outres,all,all

! Free vibration
time,1e-3
timint,on
kbc,1
fkdele,3,all
fkdele,7,all
lswrite

lssolve,1,2,1

FINISH
```

F.4 ANSYS Code for Modal Analysis Model - Top Strike

```
finish
/clear
/CWD,'D:'
/config,nres,10000

/TITLE, Modal Analysis
/FILNAME,MA,0
/triad,off
/prep7

! Everything is in meters, kilograms, Newtons, seconds!

disk_radius = 20e-3
disk_thickness = 9e-3

rod_length = 20e-3
rod_radius = 2e-3
free_length = 10e-3

rod_density = 2800
disk_density = 1800

disk_young_mod = 8.4e9
rod_young_mod = 73e9

mesh_size = rod_radius/2

! Point mass
pmass_length = mesh_size
pmass_density = 8e6

interface_thickness = 0.38e-3
interface_young_mod = 0.5e9
interface_density = 1800
```

```
! Create disk geometry
blc4,0,(-disk_thickness),disk_radius,disk_thickness
blc4,0,(free_length-rod_length),rod_radius+
    ...interface_thickness,rod_length

asba,1,2

! Create rod geometry
blc4,0,(free_length-rod_length),rod_radius,rod_length

blc4,rod_radius,-disk_thickness,interface_thickness
    ...,disk_thickness

blc4,(rod_radius-pmass_length),(free_length-
    ...pmass_length),pmass_length,pmass_length

asba,1,4

! Create point mass
blc4,(rod_radius-pmass_length),(free_length-
    ...pmass_length),pmass_length,pmass_length

aglue,all

vrotat,all,,,,,,1,6,180,8

et,1,solid92


!Interface
mp,ex,4,interface_young_mod
mp,prxy,4,0.33
mp,dens,3,interface_density

type,1
mat,4
```

```
esize,interface_thickness
vmesh,2,30,4


! Disk
mp,ex,1,disk_young_mod
mp,prxy,1,0.33
mp,dens,1,disk_density

type,1
mat,1

esize,2*mesh_size
vmesh,3,31,4

! Point Mass
mp,ex,3,rod_young_mod
mp,prxy,3,0.33
mp,dens,3,pmass_density

type,1
mat,3

esize,mesh_size/2
vmesh,1

! Rod
mp,ex,2,rod_young_mod
mp,prxy,2,0.33
mp,dens,2,rod_density

type,1
mat,2

esize,2*mesh_size
vmesh,4,32,4
vmesh,5,29,4
```

```
finish
/solu

! Modal Analysis options

ANTYPE,2
MSAVE,0
MODOPT,SUBSP,1
EQSLV,FRONT
MXPAND,1, , ,0
LUMPM,0
PSTRES,0
MODOPT,SUBSP,1,0,0, ,OFF
RIGID,SUBOPT,8,4,8,100,5,ALL

! Constrain system

da,16,all,all
da,35,all,all
da,54,all,all
da,73,all,all
da,92,all,all
da,111,all,all
da,130,all,all
da,149,all,all
da,1,symm
da,2,symm
da,4,symm
da,6,symm
da,142,symm
da,156,symm
da,151,symm
da,147,symm

solve

finish
/post1
```

```
set,list
set,first
pldisp
```

F.5 ANSYS Code for Osseointegration Loss - Dental

```
finish
/clear
/CWD,'D:'
/config,nres,10000

/TITLE, Osseointegration Loss - Dental
/FILNAME,Osseo,0
/triad,off
/prep7

! Everything is in meters, kilograms, Newtons, seconds!

disk_radius = 20e-3
disk_thickness = 9e-3

rod_length = 20e-3
rod_radius = 2e-3
free_length = 10e-3

perio_length = 20e-3
perio_radius = 1e-3

rod_density = 2800
disk_density = 1800

! Mass of Periotest rod is 9.4 grams
perio_density=0.0094/(3.14*perio_radius*perio_radius*perio_length)

disk_young_mod=8.4e9
rod_young_mod=73e9
perio_young_mod=200e9

! Osseointegration Loss
osseo_depth = 0.2e-3
```

```
fric_coef = 0.3
mesh_size = rod_radius/2

interface_thickness = 0.38e-3
interface_young_mod = 0.5e9
interface_density = 1800

! Disk and post geometry
blc4,0,(-disk_thickness),disk_radius,disk_thickness
blc4,0,(free_length-rod_length),(rod_radius+
    ...interface_thickness),rod_length

asba,1,2

k,20,0,free_length-rod_length
k,21,rod_radius,free_length-rod_length
k,22,rod_radius,-osseo_depth
k,23,rod_radius,(osseo_depth/5)
k,24,rod_radius,free_length-2*perio_radius
k,25,rod_radius,free_length
k,26,-0,free_length

a,20,21,22,23,24,25,26

! Interface geometry
blc4,rod_radius,-disk_thickness,interface_thickness,
    ...(disk_thickness-osseo_depth)
blc4,rod_radius,-osseo_depth,interface_thickness,osseo_depth

aglue,1,2
aglue,5,3
aglue,4,2
aglue,1,3


vrotat,all,,,,,,20,26,180

k,41,rod_radius,free_length k,42,rod_radius,free_length,-.001
```

```
k,43,rod_radius,free_length+.001

cskp,11,0,41,42,43
wpcsys,,11

! Periotest rod geometry
cyl4,0,-.5*perio_radius,perio_radius,,,,perio_length
blc4,0,perio_radius,-2*perio_radius,-4*perio_radius,perio_length
vsbv,9,10

csys,0
wpcsys,,0

et,1,solid92

!Interface
mp,ex,4,interface_young_mod
mp,prxy,4,0.33
mp,dens,4,interface_density
mp,mu,4,fric_coef

! Mesh size depending on amount of loss
type,1
mat,4
*if,(osseo_depth/5),LT,(3/4*interface_thickness),THEN
aesize,16,osseo_depth/4
aesize,36,osseo_depth/4
*elseif,(osseo_depth/5),GE,(3/4*interface_thickness)
aesize,16,(3/4*interface_thickness)
aesize,36,(3/4*interface_thickness)
*endif
esize,interface_thickness

vmesh,3
vmesh,7
vmesh,1
vmesh,5
```

```
! Disk
mp,ex,1,disk_young_mod
mp,prxy,1,0.33
mp,dens,1,disk_density

type,1
mat,1

esize,2*mesh_size
vmesh,2
vmesh,6

! Rod
mp,ex,2,rod_young_mod
mp,prxy,2,0.33
mp,dens,2,rod_density

type,1
mat,2

! Mesh size depending on amount of loss
aesize,22,mesh_size/4
*if,(osseo_depth/5),LT,(3/4*interface_thickness),THEN
aesize,20,osseo_depth/4
aesize,40,osseo_depth/4
*elseif,(osseo_depth/5),GE,(3/4*interface_thickness)
aesize,20,(3/4*interface_thickness)
aesize,40,(3/4*interface_thickness)
*endif
esize,2*mesh_size
vmesh,4
vmesh,8

! Perio
mp,ex,3,perio_young_mod
mp,prxy,3,0.33
mp,dens,3,perio_density
```

```
type,1
mat,3

aesize,55,mesh_size/4
esize,mesh_size
vmesh,11

! Periotest Impact
et,2,conta174
keyopt,2,7,1
keyopt,2,5,1
R,2,0,0,0.10,0,0,0
RMORE,0,0,0,0, 0,0
RMORE,0,,,, ,
RMORE,,,0,0, ,
RMORE,10

type,2
real,2
allsel,all
asel,s,area,,55
nsla,s,1
esurf
allsel,all

et,3,targe170
type,3
allsel,all
asel,s,area,,22
nsla,s,1
esurf
allsel,all

! Osseointegration
R,3,0,0,0.10,0,0,0
RMORE,0,0,0,0, 0,0
RMORE,0,,,, ,
RMORE,,,0,0, ,
```

```
RMORE,10

type,2 real,3
allsel,all
asel,s,area,,20
nsla,s,1
esurf
allsel,all

type,3
allsel,all
asel,s,area,,16
nsla,s,1
esurf
allsel,all

R,4,0,0,0.10,0,0,0
RMORE,0,0,0,0, 0,0
RMORE,0,,,, ,
RMORE,,,0,0, ,
RMORE,10

type,2 real,4
allsel,all
asel,s,area,,40
nsla,s,1
esurf
allsel,all

type,3
allsel,all
asel,s,area,,36
nsla,s,1
esurf
allsel,all


finish
```

```
/solu

ANTYPE,4

TRNOPT,full
lumpm,0

! Constrain system

da,11,all,all
da,31,all,all
da,1,symm
da,2,symm
da,4,symm
da,6,symm
da,29,symm
da,34,symm
da,37,symm
da,44,symm
da,59,uz,0
da,59,uy,0

! Transient Analysis Options

time,0.00045
timint,on
kbc,1

allsel,all
vsel,s,volu,,11
nslv,s,1
IC,all,ux,,-0.200
allsel,all

nsubst,750,750,750
autots,on
neqit,100
outres,all,all
```

```
lswrite

lssolve,1,1,1


FINISH

! Store displacement data of nodes
! down center of aluminium post

/POST26
FILE,'osseo','rst','.'

SOLU,191,NCMIT
STORE,MERGE
FILLDATA,191,,,,1,1
REALVAR,191,191

NSOL,2,44075,U,X
STORE,MERGE
XVAR,1

NSOL,3,44115,U,X
STORE,MERGE

NSOL,4,44117,U,X
STORE,MERGE

NSOL,5,44119,U,X
STORE,MERGE

NSOL,6,44121,U,X
STORE,MERGE

! Save time history variables to file data_out.dat

*GET,size,VARI,,NSETS
*DIM,DISP_VAL,TABLE,size,5
```

```
VGET,DISP_VAL(1,0),1
VGET,DISP_VAL(1,1),2
VGET,DISP_VAL(1,2),3
VGET,DISP_VAL(1,3),4
VGET,DISP_VAL(1,4),5
VGET,DISP_VAL(1,5),6

*CFOPEN,0p2_mm_osseo_out,dat
*VWRITE,'TIME','TOP','DOWN_1','DOWN_2','DOWN_3','DOWN_4'
%14C %14C %14C %14C %14C %14C
*VWRITE,DISP_VAL(1,0),DISP_VAL(1,1),DISP_VAL(1,2),DISP_VAL(1,3),
    ...DISP_VAL(1,4),DISP_VAL(1,5)
%14.5G %14.5G %14.5G %14.5G %14.5G %14.5G
*CFCLOSE
```